공학박사 학위논문

Hydrogen Production by Steam Reforming of Natural Gas over Mesoporous Nickel/Alumina Catalysts

중형기공성 니켈/알루미나 촉매 상에서 수증기 개질 반응을 통한 수소 생산

2018년 2월

서울대학교 대학원

화학생물공학부

유 재 경

Abstract

Hydrogen Production by Steam Reforming of Natural Gas over Mesoporous Nickel/Alumina Catalysts

Jaekyeong Yoo

School of Chemical and Biological Engineering

The Graduate School

Seoul National University

With increasing concerns about the depletion of fossil fuels and global warming, various researches on sustainable and renewable energy have attracted much attention. Hydrogen has been considered as one of the most advantageous energy carriers because of its high energy density, eco-friendliness, and abundance. Steam reforming of natural gas is the predominant means of producing hydrogen due to its high hydrogen conversion efficiency and excellent economical advantage. Nickel-based catalysts are known to show high activity in the steam reforming of natural gas. However, nickel-based catalysts retain weak resistance toward catalyst deactivation caused by nickel sintering and carbon deposition. Therefore, it is

important to develop a new preparation method for nickel-based catalyst to achieve high catalytic activity and enhanced stability in the steam reforming of natural gas.

In this work, in order to achieve efficient catalyst system for steam reforming of natural gas, mesoporous nickel/alumina catalysts were designed by various catalyst compositions such as the addition of alkaline earth metal and vanadium, and preparation methods such as a supercritical CO_2 drying method and the use of butyric acid.

First, A series of mesoporous alkaline earth metal-promoted nickel-alumina xerogel (M/NA, M = Mg, Ca, Sr, and Ba) catalysts were prepared by a single-step epoxide-driven sol-gel method and a subsequent incipient wetness impregnation method. For reference, a nickel-alumina xerogel catalyst without promoter (NA) was prepared by a single-step epoxide-driven sol-gel method. Hydrogen chemisorption analyses showed that nickel surface area of reduced catalysts decreased in the order of Mg/NA > Sr/NA > Ca/NA > NA > Ba/NA. In the hydrogen production by steam reforming of natural gas, the catalytic performance of NA and M/NA catalysts was well correlated with the nickel surface area of the catalysts; natural gas conversion and hydrogen yield increased with increasing nickel surface area. Among the catalysts tested, Mg/NA catalyst with the highest nickel surface area showed the best catalytic performance. The amount of carbon deposition on the used M/NA catalysts was less than that on the used NA catalyst.

In order to improve the best catalyst Mg/NA above, magnesium-doped mesoporous nickel-alumina aerogel catalyst (Mg/NAA) was prepared by a single-step epoxide-driven sol-gel method and a subsequent supercritical CO_2

drying followed by an incipient wetness impregnation method. For comparison, magnesium-doped mesoporous nickel-alumina xerogel catalyst (Mg/NAX) was prepared by the similar method of Mg/NA above. Surface area, pore volume, and average pore dimeter of Mg/NAA catalysts were larger than those of Mg/NAX catalyst due to suppressed collapse of nickel-alumina gel network during the drying step. Nickel surface area and nickel dispersion of reduced catalysts were better in Mg/NAA catalyst than in Mg/NAX catalyst. In the CH_4-TPD analyses, CH_4 affinity of Mg/NAA catalyst was higher than that of Mg/NAX catalyst. In the hydrogen production by steam reforming of natural gas, Mg/NAA catalyst with the higher nickel dispersion and high CH_4 affinity showed the better catalytic performance than Mg/NAX catalyst in terms of natural gas conversion and hydrogen yield.

Vanadium-nickel-alumina catalysts with different vanadium loading (xVNA, x = 0, 0.5, 1.0, 1.5, and 2.0) were prepared by a single-step sol-gel method. TPR analyses revealed that the addition of vanadium increased reducibility of xVNA catalysts. From XRD analyses of reduced xVNA catalysts, it was found that an appropriate amount of vanadium reduced nickel crystallite size. In the hydrogen production by steam reforming of natural gas, natural gas conversion and hydrogen yield showed volcano-shaped trends with respect to vanadium loading. Among the catalysts, vanadium-nickel-alumina catalyst with 1.0 wt% vanadium, which retained the smallest crystallite size of metallic nickel, showed the best catalytic performance.

A series of butyric acid (BA)-assisted nickel/alumina catalysts (denoted as xBAN/A) with different butyric acid/Ni molar ratio (x) were prepared by an impregnation method. xBAN/A catalysts with an appropriate amount of

butyric acid showed the enhanced nickel dispersion because of steric hindrance of butyric acid shell surrounding nickel particle. Addition of butyric acid also increased methane adsorption capacity of the catalysts, which was directly related to the catalytic performance. In the steam reforming of natural gas, both natural gas conversion and hydrogen yield showed volcano-shaped trends with respect to butyric acid/Ni molar ratio (x). Natural gas conversion and hydrogen yield increased with increasing nickel dispersion. Among the catalysts tested, 0.25BAN/A catalyst with the highest nickel dispersion exhibited the best catalytic performance in the steam reforming of natural gas.

In summary, various nickel/alumina catalysts were designed to produce hydrogen by steam reforming of natural gas. In order to investigate the effect of physicochemical properties of the catalysts on catalytic performance in the steam reforming of natural gas, several characterizations such as N_2 adsorption-desorption, XRD, TPR, TEM, SEM, H_2-TPD, CH_4-TPD, and FT-IR analyses were conducted. It was concluded that nickel dispersion played a crucial role in determining the catalytic performance in the hydrogen production by steam reforming of natural gas.

Keywords: Hydrogen production, Steam reforming of natural gas, Nickel catalyst, Alkaline earth metal, Supercritical CO_2 drying, Vanadium, Butyric acid

Student Number: 2015-30216

Contents

List of Tables

List of Figures

Chapter 1. Introduction

1.1. Hydrogen energy

With increase in human population, global energy consumption increases every year [1,2]. The rapid population growth also causes imprudent industrial expansion, leading to serious environmental problems such as global warming and climate change [3-6]. Present energy supply methods based on oil industries are expected to lose their utility values due to oil limitation and carbon-constraining policies. Therefore, it is urgent to invest and develop sustainable alternative energy sources such as wind, hydroelectric power, geothermal heat, solar light, nuclear power, vegetable oil, and hydrogen.

Among the various form of energy sources, hydrogen is regarded as one of the most important alternative energy carriers for the future. Hydrogen is abundantly available from various sources and has the highest energy content per unit of weight (> 140 kJ/g) than any other known fuels (Table 1.1) [7]. Besides, hydrogen is clean and renewable fuel, because it does not release any pollutant such as NO_x, SO_x, and particulate matter during the combustion process. For these reasons, it is expected that upto 65% on the total energy demand would be shared by hydrogen in 2050 (Table 1.2) [8]. Therefore, investigation and optimization of hydrogen production method for stable and efficient hydrogen supply is of great importance.

Table 1.1

Energy density and hydrogen to carbon ratio of various fuels

Fuel	Energy density (MJ/kg)	H/C ratio
Hydrogen	142.0	-
Natural gas	55.5	4.0
LPG	50.0	2.5-2.7
Methanol	22.5	4.0
Biogas (from gasifier)	4-14	0.7-2.0
Ethanol	29.7	3.0
Gasoline	45.8	1.6-2.1
Jet fuel	46.3	1.6-2.0
Diesel	45.3	1.8-2.3

Table 1.2

Share of individual primary energy sources (%)

Source of energy	1998	2025	2050
Fossil fuels	88	62	29
Nuclear energy	10	2	2
Hydrogen from solar energy	-	7	31
Electricity from solar energy	-	11	16
Heat from solar energy	-	18	22
Energy from solar energy	2	25	35
Hydrogen	-	11	34

Fig. 1.1. Applications of hydrogen.

1.2. Steam reforming of natural gas

Most of hydrogen used in the world is produced by steam reforming processes, corresponding to the production of 96% of on-purpose hydrogen [9]. Natural gas, which is mainly composed of methane and ethane, is the most widely utilized hydrogen source in the steam reforming process because of its abundance. Steam reforming of natural gas can be described by the following equations.

$$CH_4 + H_2O \leftrightarrow CO + 3H_2 \qquad \Delta H^{o}_{298\ K} = +206.1\ kJ/mol \qquad (1.1)$$

$$C_2H_6 + 2H_2O \leftrightarrow 2CO + 5H_2 \qquad \Delta H^{o}_{298\ K} = +347.3\ kJ/mol \qquad (1.2)$$

$$CO + H_2O \leftrightarrow CO_2 + H_2 \qquad \Delta H^{o}_{298\ K} = -41.2\ kJ/mol \qquad (1.3)$$

Equations (1.1) and (1.2) represent steam reforming reactions to produce CO and H_2 from methane and ethane, respectively. Water-gas shift reaction (Equation (1.3)) accompanied by the reforming reactions allows an additional hydrogen production. Overall reactions in the presence of abundant water can be expressed as follows.

$$CH_4 + 2H_2O \leftrightarrow CO_2 + 4H_2 \qquad \Delta H^{o}_{298\ K} = +164.9\ kJ/mol \qquad (1.4)$$

$$C_2H_6 + 4H_2O \leftrightarrow 2CO_2 + 7H_2 \qquad \Delta H^{o}_{298\ K} = +264.9\ kJ/mol \qquad (1.5)$$

According to the equations, steam reforming of natural gas is a highly endothermic reaction. Thus, typical steam reforming process is carried out at

around 800 ^{o}C to supply large amount of energy [10]. Such a high-temperature operation reduces competitiveness in hydrogen production market, and it is a serious obstacle to commercialize small size reformers for fuel cells. In this respect, it is important to reduce the reaction temperature for steam reforming of natural gas. However, low-temperature steam reforming reaction over commercial nickel-based catalysts has some drawbacks such as low catalytic activity and severe carbon deposition [9].

To overcome these problems, many researches have attempted to modify nickel-based reforming catalysts as follows:

- Li-, Na-, and K-doped Ni-containing smectite-type catalyst showed high catalytic performance in the steam reforming of acetic acid, yielding more metallic Ni species than undoped catalysts [11].
- Mg- and Ca-modified CuNi/$MgSiO_2$ and CuNi/$CaSiO_2$ catalysts also exhibited an enhanced catalytic performance and low carbon deposition in the steam reforming of ethanol due to highly dispersed Ni particles formed by strong metal-support interaction [12].
- A Ni/Sr/ZrO_2 catalyst showed high activity and stability in the steam reforming of hydrocarbons due to the formation of mixed oxide species which prevented carbon accumulation and sintering of Ni particles [13]
- It has been reported that an ordered mesoporous support suppressed sintering of active metal species due to confinement effect of separated mesoporous channels [14].
- It has also been reported that a nickel catalyst coated with silica

overlayer exhibited an enhanced catalyst stability in the carbon dioxide reforming of methane [15].

- Nguyen et al. used nickel/zirconia catalysts with different nickel loading for steam reforming of methane [16]. They reported that a catalyst with 15 wt% nickel loading exhibited the best catalytic performance because too much amount of nickel loading blocked pore of the catalysts.
- Another research reported the effect of ceria on the support of nickel/zirconia catalyst [17]. According to this research, nickel/ceria-zirconia catalysts showed an excellent catalytic performance and high resistant toward coke deposition because of the enhanced water-gas shift reaction.
- In addition, various kinds of second metal-doped catalysts have also been tested for steam reforming reaction. Wu et al. reported that the addition of small amount of second metal such as Au, Ag, Sn, Cu, and Co to nickel-based catalysts modified properties of nickel particles, enhancing selectivity to hydrogen and resistance toward carbon formation [18].
- Christensen et al. have reported that nickel catalysts supported on hydrotalcite materials showed the enhanced coke resistance with decreasing nickel particle size during the steam reforming of methane [19].
- Zhu et al. have also reported that addition of Mg into nickel-silica catalyst induced high dispersion of active phase and inhibition of metal

sintering, resulting in high catalytic activity and stability during the dry reforming of methane [20].

- An ordered mesoporous nickel-alumina catalyst prepared with a structure modifier (trimethylbenzene) showed the enhanced mesoporous structure and formed small metallic nickel [21]. The modified catalyst exhibited a stronger resistance toward nickel sintering and a better catalytic performance than nickel-alumina catalyst without modifier during the steam reforming of methane.
- It has been reported that addition of fatty acid into precursor solution increased nickel dispersion of nickel/silica catalysts prepared by an impregnation method, and the catalysts showed high catalytic activity and stability during the dry reforming of methane [22].

1.3. Objective

Nickel-based reforming catalysts are vulnerable to catalyst deactivation due to carbon deposition and nickel sintering during the reaction. Therefore, it is important to develop a new nickel-based catalyst to achieve high catalytic activity and enhanced stability in the steam reforming of natural gas. It is known that catalytic performance of the catalysts are greatly influenced by several physicochemical properties such as surface area, porosity, crystalline structure, reducibility, nickel dispersion, and methane adsorption capacity. Especially, nickel dispersion of reduced catalysts is known to be a crucial factor determining overall reaction rate and hydrogen yield. In this work, therefore, various modifications of mesoporous nickel/alumina catalysts have been attempted to improve both catalytic activity and stability in the steam reforming of natural gas by enhancing nickel dispersion.

It is known that various kinds of metal retain promotion effect on nickel-based catalysts. Thus, it is expected that the introduction of alkali and alkaline earth metal into nickel-based catalysts may improve the catalytic performance and stability in the steam reforming of natural gas by changing the formation environment of Ni particles. However, any comparative studies on the addition of alkaline earth metals (Mg, Ca, Sr, and Ba) as promoters to nickel-based catalysts for steam reforming of natural gas have not been attempted yet. Therefore, a systematic investigation on the addition of alkaline earth metal to mesoporous nickel/alumina catalyst prepared by a single-step epoxide-driven sol-gel method would be worthwhile.

It is known that well-developed mesoporous nickel-based catalysts retained excellent catalytic activity during the reforming reactions due to high mass transfer rate of reactant molecules and finely dispersed nickel particles [23]. Aerogel-based catalysts with outstanding textural properties compared to xerogel-based catalysts showed high and stable catalytic activity in the steam reforming reactions in the previous study [24]. However, a mesoporous magnesium-doped nickel-alumina aerogel catalyst prepared by an epoxide-driven sol-gel method has never been applied for hydrogen production by steam reforming of natural gas. Therefore, it is worthwhile to investigate physicochemical properties and the catalytic performance of mesoporous magnesium-doped nickel-alumina aerogel catalyst in the steam reforming of natural gas.

It has also been reported that vanadium doping inhibits sintering of nickel by suppressing nickel mobility [25]. However, mesoporous vanadium-nickel-alumina catalysts have never been applied for hydrogen production by steam reforming of natural gas. It is expected that nickel dispersion on nickel-alumina catalysts, which is an important factor involved in catalytic performances in the steam reforming reaction, could be controlled by adjusting the amount of vanadium. In this point of view, preparation of mesoporous vanadium-nickel-alumina xerogel catalysts with different vanadium loading for practical application to hydrogen production by steam reforming of natural gas was carried out.

Generally, conventional impregnation method is unfavorable to disperse active component onto support. In order to increase dispersion of active component, butyric acid-assisted impregnation method has been studied.

Butyric acid-assisted impregnation method involves formation of butyric acid shell surrounding nickel particle due to the charge difference between nickel and butyric acid. Steric hindrance of butyric acid shell repulse each nickel particle, resulting in fine dispersion of active metal on support. To our best knowledge, however, no study has been conducted on nickel/alumina catalyst prepared by epoxide-driven sol-gel method and subsequent butyric acid-assisted impregnation method. Thus, design of nickel/alumina catalyst by butyric acid-assisted impregnation method for steam reforming of natural gas would be worthwhile.

Chapter 2. Experimental

2.1. Preparation of catalysts

2.1.1. Preparation of mesoporous alkaline earth metal-doped nickel-alumina xerogel catalyst

A series of mesoporous alkaline earth metal-promoted nickel-alumina xerogel catalysts were prepared by a single-step epoxide-driven sol-gel method and a subsequent incipient wetness impregnation. 20.3 g of aluminum precursor (aluminum nitrate nonahydrate, Junsei, 98%) and 2.7 g of nickel precursor (nickel nitrate hexahydrate, Sigma-Aldrich, 97%) were dissolved in ethanol (119 ml) with vigorous stirring to obtain a nickel-alumina composite sol. 51 ml of propylene oxide (Acros Organics, 99%) was then added into the solution as a gelation agent to induce polycondensation reaction between Al^{3+} and Ni^{2+} ions. The molar ratio of aluminum precursor:nickel precursor:propylene oxide was fixed at 1:0.17:13.5. After maintaining the solution for a few minutes, a green opaque nickel-alumina composite gel was obtained. The gel was aged for 36 h, and it was then dried at 80 ^{o}C for 24 h in a convection oven. The resulting powder was calcined at 700 ^{o}C for 5 h to yield a mesoporous nickel-alumina xerogel catalyst (denoted as NA). For addition of alkaline earth metals onto NA catalyst, alkaline earth metal precursor solutions containing magnesium nitrate hexahydrate (Junsei, 99%),

calcium nitrate tetrahydrate (Junsei, 98%), strontium nitrate (Sigma-Aldrich, 99%), and barium nitrate (Junsei, 99%) were separately dissolved in deionized water. Each alkaline earth metal precursor solution was then introduced to NA by an incipient wetness impregnation method. The impregnated sample was dried at 100 °C for 1 h, and finally, it was calcined at 700 °C for 5 h. The prepared catalysts were denoted as M/NA (M = Mg, Ca, Sr, and Ba). Nickel loading on NA and M/NA catalysts was fixed at 20 wt%, and alkaline earth metal loading on M/NA catalysts was fixed at 2 wt%.

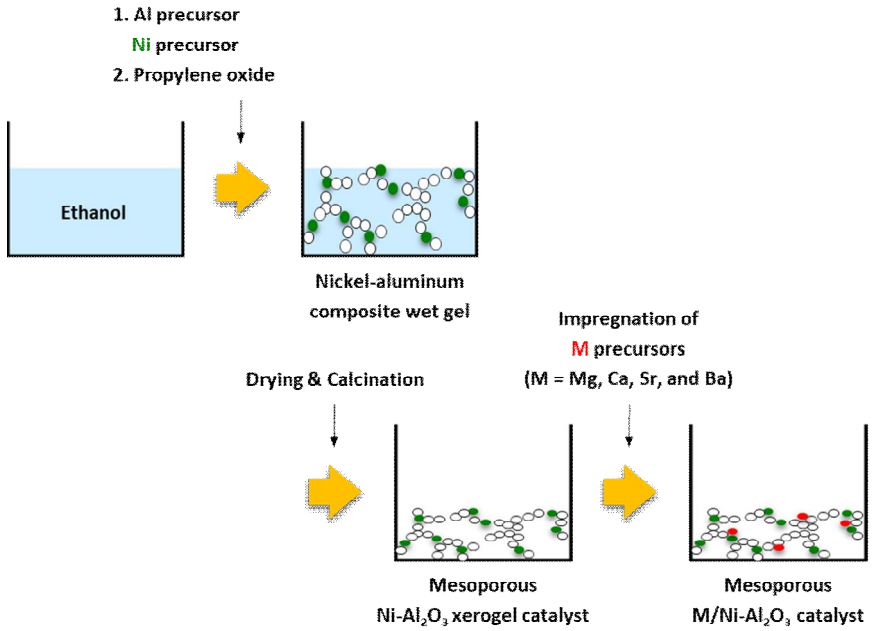

Fig. 2.1. Schematic procedures for the preparation of M/NA catalysts by an epoxide-driven sol-gel method followed by an impregnation method.

2.1.2. Preparation of mesoporous nickel-alumina aerogel catalyst by a supercritical CO_2 drying method

A magnesium-doped nickel-alumina aerogel catalyst was prepared by a single-step epoxide-driven sol-gel method and a supercritical CO_2 drying followed by an incipient wetness impregnation. 20.3 g of aluminum nitrate nonahydrate (Junsei, 98%) and 2.7 g of nickel nitrate hexahydrate (Sigma-Aldrich, ≥ 97%) were dissolved in ethanol (119 ml). The solution was stirred for 20 min to obtain a nickel-alumina composite sol. 51 ml of propylene oxide (Acros Organics, 99%) was then added into the solution as a gelation agent to initiate polycondensation reaction between metal species. After a few minutes, a green opaque nickel-alumina composite gel was obtained. The resulting gel was aged at room temperature for 36 h, and it was then washed with ethanol several times. The gel was transferred to an autoclave, and supercritical carbon dioxide drying was done at 50 ^{o}C and 100 bar for 2 h. The resulting powder was calcined at 700 ^{o}C for 5 h to obtain nickel-alumina aerogel catalyst. For addition of magnesium promotor, magnesium nitrate hexahydrate (Junsei, 99%) was dissolved in deionized water. The magnesium precursor solution was then introduced to the nickel-alumina aerogel catalyst by an incipient wetness impregnation method. The impregnated sample was dried at 100 °C for 1 h. Finally, the dried sample was calcined at 700 °C for 5 h. The prepared catalyst was denoted as Mg/NAA. Nickel loading and magnesium loading on Mg/NAA catalyst was 20 wt% and 2 wt%, respectively.

For comparison, a magnesium-doped nickel-alumina xerogel catalyst (denoted as Mg/NAX) with 20 wt% nickel loading and 2 wt% magnesium loading was also prepared by the similar methods described above. The only difference was that Mg/NAX catalyst was dried by conventional evaporative drying at 80 ^{o}C for 48 h in a convection oven instead of supercritical CO_2 drying.

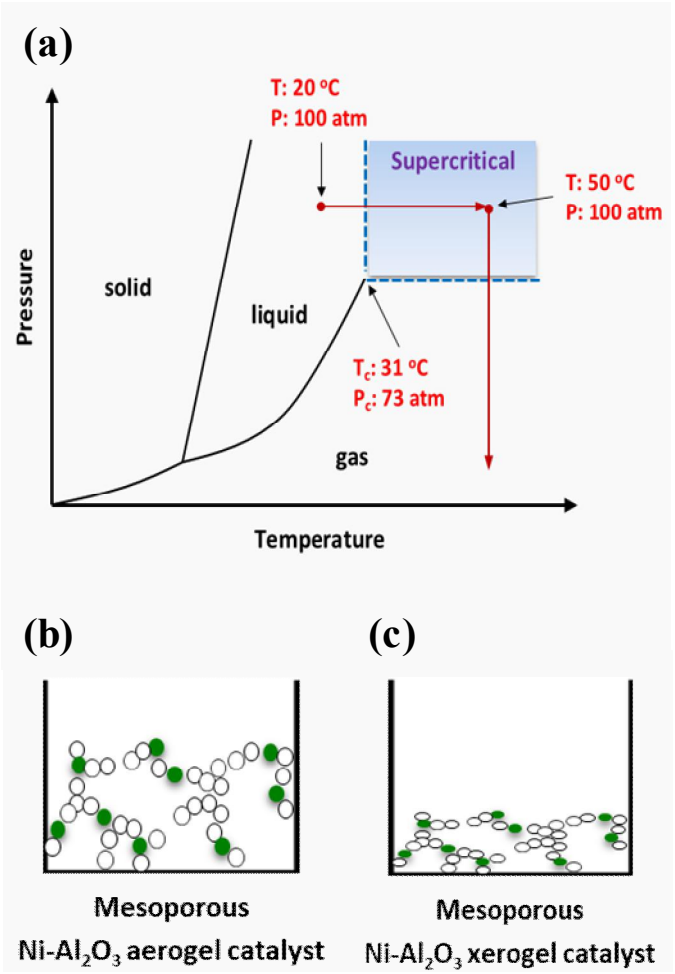

Fig. 2.2. (a) Supercritical CO_2 drying process expressed on phase diagram, and schematic morphology of (b) aerogel catalyst and (c) xerogel catalyst.

2.1.3. Preparation of mesoporous vanadium-nickel-alumina xerogel catalyst

Vanadium-nickel-alumina catalysts with different vanadium loading were prepared by a sol-gel method. 7.36 g of aluminum nitrate nonahydrate (Junsei, 98%), 1.02 g of nickel nitrate hexahydrate (Sigma-Aldrich, ≥ 97%), and different amount of ammonium metavanadate (Sigma-Aldrich, ≥ 99+%) were dissolved in 54 ml of ethanol. 10 ml of distilled water containing 0.2 ml of nitric acid (PFP, 69%) was added to the solution, and it was stirred overnight for complete dissolution of metal precursors. 16.2 ml of propylene oxide (Acros Organics, 99%) was then added to the solution to make a soft gel composite by hydrolysis and condensation reactions. The gel was aged at room temperature for 48 h. The obtained gel was crushed into small pieces and washed by absolute ethanol (Fisher, 99.9%) several times. The washed gel was then dried at 80 ^{o}C for 48 h. The grain of dried gel was mashed into powder by a mortar and pestle, and finally, it was calcined at 700 ^{o}C for 5 h. The nickel loading was kept at 20 wt% and vanadium loading was varied from 0 to 2 wt%. The prepared vanadium-nickel-alumina catalysts were denoted as xVNA (x = 0, 0.5, 1.0, 1.5, and 2.0), where x represented the vanadium loading (wt%).

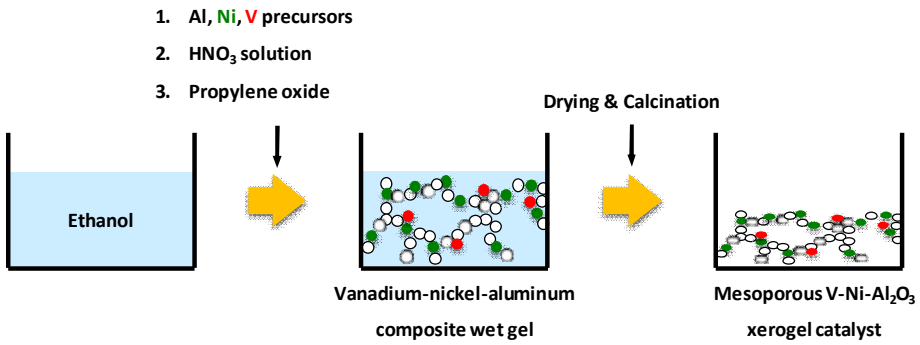

Fig. 2.3. Schematic procedures for the preparation of xVNA catalysts.

2.1.4. Preparation of mesoporous nickel/alumina catalyst by a butyric acid-assisted impregnation method

Alumina support was preliminarily prepared via a sol-gel method. 25.7 g of aluminum nitrate nonahydrate (Junsei, 98%) was dissolved in 160.5 ml of ethanol. 48.6 ml of propylene oxide (Samchun, 99%) was introduced to the aluminum precursor solution as a gelation agent. The mixed solution turned into a white gel composite after a few minutes. The gel was aged at room temperature for 2 days. The obtained gel was crushed into small pieces and washed with anhydrous ethanol. The gel was then placed in a convection oven at 80 ^{o}C for 2 days for drying. The obtained matter was grinded into powder using a mortar and pestle. The powder was calcined at 700 ^{o}C for 5 h.

A series of butyric acid (BA)-assisted mesoporous nickel/alumina catalysts were prepared via an impregnation method. 0.51 g of nickel nitrate hexahydrate (Sigma-Aldrich, $\geq$97%) was dissolved in 10 ml of D.I. water, and different amount of butyric acid was dropped to the nickel precursor solution. The mixed solution was heated to 80 ^{o}C, and 1.0 g of alumina support was added into the solution. Water was then evaporated at 80 ^{o}C with vigorous stirring. The obtained grain was dried at 80 ^{o}C overnight, and it was calcined at 700 ^{o}C for 5 h. Nickel loading was kept at 10 wt% in all the catalysts, and butyric acid (BA)/Ni molar ratio was varied from 0 to 1. The prepared catalysts were denoted as xBAN/A (x = 0, 0.1, 0.25, 0.5, and 1), where x represented the butyric acid (BA)/Ni molar ratio.

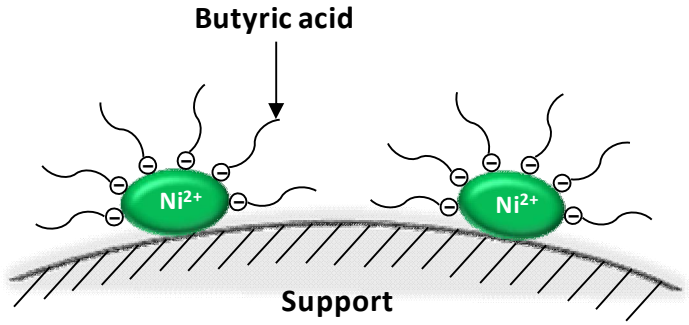

Fig. 2.4. The proposed promotion mechanism of butyric acid during an impregnation method.

2.2. Characterization

2.2.1. Physicochemical properties

In order to determine the actual chemical compositions of the catalysts, inductive coupled plasma atomic emission spectroscopy (ICP-AES) analyses were conducted with an ICPS-1000IV (Shimadzu) instrument.

N_2 adsorption-desorption analyses were conducted at -196 ^oC to measure surface area, pore volume, and pore diameter of the catalysts (BELSORP-mini II, BEL Japan). The Brunauer-Emmett-Teller (BET) method was used to calculate surface area of the catalysts. Prior to the measurement, each sample was degassed at 150 ^oC for 5-6 h.

2.2.2. Crystalline structure

Crystalline phases of the calcined and reduced catalysts were determined by X-ray diffraction (XRD) analyses with a D-Max2500-PC diffractometer (Rigaku) using Cu-Ka radiation (λ = 1.541 Å) operated at 50 kV and 100 mA. For the XRD measurements of reduced catalysts, the calcined catalysts were reduced *ex-situ* under hydrogen flow at 700 ^oC for 3 h.

2.2.3. Reducibility

Temperature-programmed reduction (TPR) experiments were carried

out in order to examine metal-support interaction of the catalysts. Each calcined catalyst sample was charged into a U-shaped quartz reactor, and it was reduced using a reducing gas mixture of hydrogen (2 ml/min) and nitrogen (20 ml/min) at a heating rate of 5 ^{o}C/min from room temperature to 1000 ^{o}C. TPR profiles of the catalysts were obtained using a thermal conductivity detector (TCD).

2.2.4. Morphological feature

Transmission electron microscopy (TEM) analyses were performed to examine morphology and nickel dispersion of the catalysts using JEM-2100 (JEOL) operated at 200 kV. High-resolution transmission electron microscopy (HR-TEM) experiments were carried out in order to examine the nickel dispersion and lattice fringe of the reduced catalysts using a JEM-3010 (JEOL) apparatus operated at 300 kV. Prior to the TEM analyses, the catalysts were reduced *ex-situ* under hydrogen flow at 700 ^{o}C for 3 h.

Morphology and elemental distribution of the calcined catalysts were examined by scanning electron microscopy-energy dispersive spectroscopy (SEM-EDS) mapping analyses using JSM-6701F (JEOL)..

2.2.5. H_2 and CH_4 chemisorption studies

Hydrogen chemisorption measurements were performed with a BELCAT-B (BEL Japan) instrument to measure the nickel dispersion and

nickel surface area of the reduced catalysts. Prior to the measurements, each catalyst was reduced *in-situ* under 5 mol% H_2/Ar gas (50 ml/min) at 700 ^oC for 3 h, and then the catalyst was purged with pure Ar (50 ml/min) at 700 ^oC for 5 min. After the catalyst was cooled to 50 ^oC under Ar flow, the amount of hydrogen uptake was determined by periodically injecting 5 mol% H_2/Ar gas. The amount of adsorbed hydrogen was calculated by assuming that one hydrogen atom occupies one surface nickel atom.

Hydrogen temperature-programmed desorption (H_2-TPD) analyses were performed to measure nickel dispersion (BELCAT-B, BEL Japan). Each calcined catalyst (50 mg) was preliminarily reduced under a reducing gas of 5% hydrogen diluted with argon (50 ml/min) at 700 ^oC for 3 h. Hydrogen adsorption was carried out under a 5% hydrogen flow diluted with argon (50 ml/min) at 50 ^oC for 30 min. Physisorbed molecules was eliminated by purging with an argon gas (50 ml/min) at 100 ^oC for 1 h. Desorption of chemisorbed molecules was monitored at 5 ^oC/min to 950 ^oC under an argon flow (30 ml/min). A TCD was employed to detect the desorbed hydrogen.

In Section 3.2 and 3.4, methane adsorption capacity of the catalysts was measured by performing CH_4-TPD experiments. In Section 3.2, 25 mg of each catalyst sample was reduced at 700 ^oC for 3 h by a hydrogen flow (3 ml/min) diluted with helium (30 ml/min) using a continuous flow fixed-bed apparatus. After cooling the sample to room temperature under a helium flow (5 ml/min), 20 ml of methane was pulsed into the reactor for 10 times to saturate active sites with methane. Physisorbed methane was removed by purging the sample at 50 ^oC for 1 h under a flow of helium (15 ml/min). The measurement was conducted under a helium flow (15 ml/min) by increasing temperature from

50 ^{o}C to 900 ℃ at a heating rate of 10 °C/min. The desorbed methane was detected using a GC-MSD (6890N GC-5975MSD, Agilent). In Section 3.4, CH_4-TPD was performed using BELCAT-B (BEL Japan). Each calcined catalyst (50 mg) was preliminarily reduced under a reducing gas of 5% hydrogen diluted with argon (50 ml/min) at 700 ^{o}C for 3 h. Methane adsorption was carried out at 50 ^{o}C under a mixed gas of 1% methane diluted with argon (50 ml/min) at 50 ^{o}C for 30 min. Elimination of physisorbed methane was performed by purging with an argon gas (50 ml/min) at 250 ^{o}C for 1 h. Desorption of chemisorbed methane was monitored at 5 ^{o}C/min within temperature range of 200-1000 ^{o}C under an argon flow (30 ml/min).

2.2.6. Carbon deposition on used catalysts

Carbon, hydrogen, nitrogen, and sulfur (CHNS) elemental analyses were conducted with a CHNS 932 (Leco) instrument to quantify the amount of carbon deposition on the used catalysts.

2.2.7. Chemical states of elements

In order to investigate chemical state of butyric acid, infrared spectra of as-prepared catalysts were obtained using a Fourier transform infrared (FT-IR) spectrometer (ThermoScientific, Nicolet 6700) with a diffuse reflectance accessory. FT-IR spectra were recorded within the spectral range of 3500-650 cm^{-1}.

2.3. Hydrogen production by steam reforming of natural gas

Steam reforming of natural gas was conducted in a fixed-bed quartz reactor. Each catalyst was preliminarily reduced under a reducing gas of hydrogen (3 ml/min) and nitrogen (30 ml/min) at 700 ^{o}C for 3 h. Steam reforming of natural gas was then carried out at 550-600 ^{o}C. A feed stream composed of natural gas, steam, and nitrogen was used during the reaction. Composition of natural gas was 92 vol% methane and 8 vol% ethane. The effluent gas was periodically sampled and analyzed using a gas chromatograph (ACME 6000, Younglin). The sampled gas was separated through Molecular Sieve 5A (60/80 mesh, 2 ft x 1/8" x 2mm ID) and Porapak N (80/100 mesh, 20 ft x 1/8" x 2mm ID) columns. Each separated component was detected by a TCD. Conversion of natural gas and yield for hydrogen were defined as follows. *Fi* represents the molar flow rate of *i* species.

$$Natural\ gas\ conversion\,(\%) = \frac{F_{CH_4,in} + F_{C_2H_6,in} - F_{CH_4,out} - F_{C_2H_6,out}}{F_{CH_4,in} + F_{C_2H_6,in}} \times 100 \tag{2.1}$$

$$Hydrogen\ yield\ (\%) = \frac{F_{H_2,out}}{2 \times F_{CH_4,in} + 3 \times F_{C_2H_6,in}} \times 100 \tag{2.2}$$

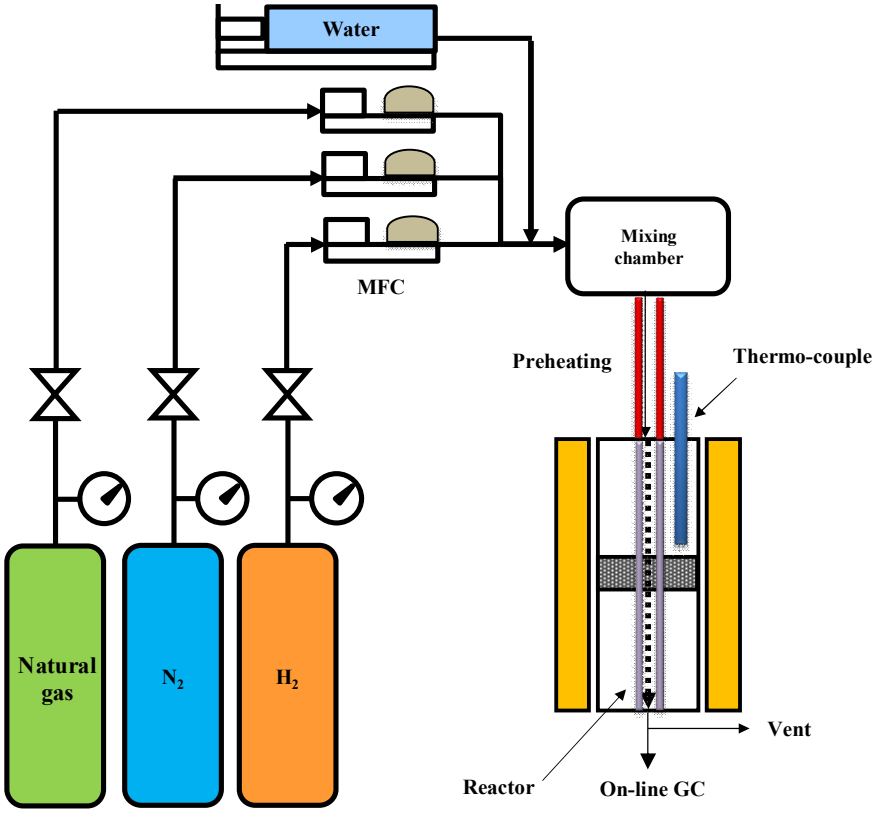

Fig. 2.5. Scheme for the steam reforming of liquefied natural gas reactor system.

Table 2.1

Steam reforming reaction conditions

	Reaction temperature (°C)	Catalyst weight (mg)	S/C molar ratio	Total flow rate (ml/h · g-cat.)
Section 3.1	600	100	2.1	27,000
Section 3.2	600	15	2.1	180,000
Section 3.3	550	50	2.1	41,390
Section 3.4	550	50	2.1	41,390

Chapter 3. Results and Discussion

3.1. Mesoporous alkaline earth metal-doped nickel-alumina xerogel catalyst

3.1.1. Textural properties of calcined catalysts

Fig. 3.1 shows the nitrogen adsorption-desorption isotherms of calcined NA and M/NA (M = Mg, Ca, Sr, and Ba) catalysts. It was found that all the catalysts exhibited type-IV isotherms with H2-type hysteresis loops, indicating the formation of mesoporous structure with "ink-bottle" pores [26]. Detailed physicochemical properties of the catalysts are summarized in Table 3.1. All the catalysts showed high surface area (> 250 m^2/g), large pore volume (> 0.4 cm^3/g), and large average pore diameter (> 6.0 nm) within mesopore range. It is noteworthy that surface area and pore volume of M/NA catalysts were smaller than those of NA catalyst. This indicates that some mesopores in the M/NA catalysts were partly blocked by alkaline earth metals during the impregnation step [27,28]. The measured nickel and alkaline earth metal contents of NA and M/NA catalysts were in good agreement with the theoretical values.

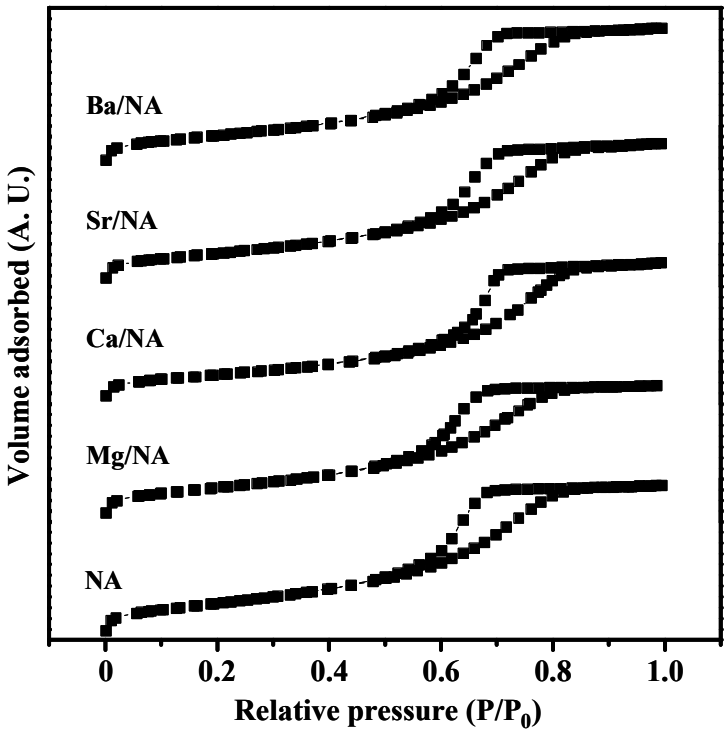

Fig. 3.1. Nitrogen adsorption-desorption isotherms of calcined NA and M/NA catalysts.

Table 3.1

Physicochemical properties of calcined NA and M/NA catalysts

Catalyst	Measured Ni Loading (wt%)[a]	Measured M Loading (wt%)[a]	Surface area (m^2/g)[b]	Pore volume (cm^3/g)[c]	Average pore diameter (nm)
NA	20.2	-	316	0.53	6.7
Mg/NA	20.1	2.4	301	0.50	6.6
Ca/NA	19.2	2.1	255	0.51	8.0
Sr/NA	20.0	2.6	287	0.52	7.2
Ba/NA	20.3	2.4	289	0.51	7.0

[a] Determined by ICP-AES measurement

[b] Calculated by the BET equation

[c] Total pore volume at $P/P_0 \sim 0.990$

3.1.2. Crystalline structures of calcined catalysts

Fig. 3.2 shows the XRD patterns of NA and M/NA (M = Mg, Ca, Sr, and Ba) catalysts calcined at 700 ^{o}C for 5 h. XRD patterns of NA catalyst was almost identical to those of M/NA catalysts, indicating that the introduction of alkaline earth metal did not affect the crystalline structure of M/NA catalysts. No characteristic diffraction peaks corresponding to bulk nickel oxide were observed in all the catalysts. Instead, all the catalysts showed three diffraction peaks indicative of nickel aluminate phase (solid lines in Fig. 3.2). Furthermore, the diffraction peak of $NiAl_2O_4$ at $2\theta = 65.5^{o}$ was clearly observed, representing the lattice expansion of γ-Al_2O_3 (440) (dashed line in Fig. 3.2 at $2\theta = 67.0^{o}$). This is because Ni^{2+} ions were incorporated into the cationic deficient sites of γ-Al_2O_3, resulting in the formation of nickel aluminate phase in the NA and M/NA catalysts [29,30]. Thus, it is inferred that most of the nickel species existed in the form of nickel aluminate phase in the NA and M/NA catalysts. It should be noted that no distinctive diffraction peaks for alkaline earth metal (M) oxides were observed in all the M/NA catalysts, because only a small amount (< 2 wt%) of alkaline earth metal was loaded on the M/NA catalysts.

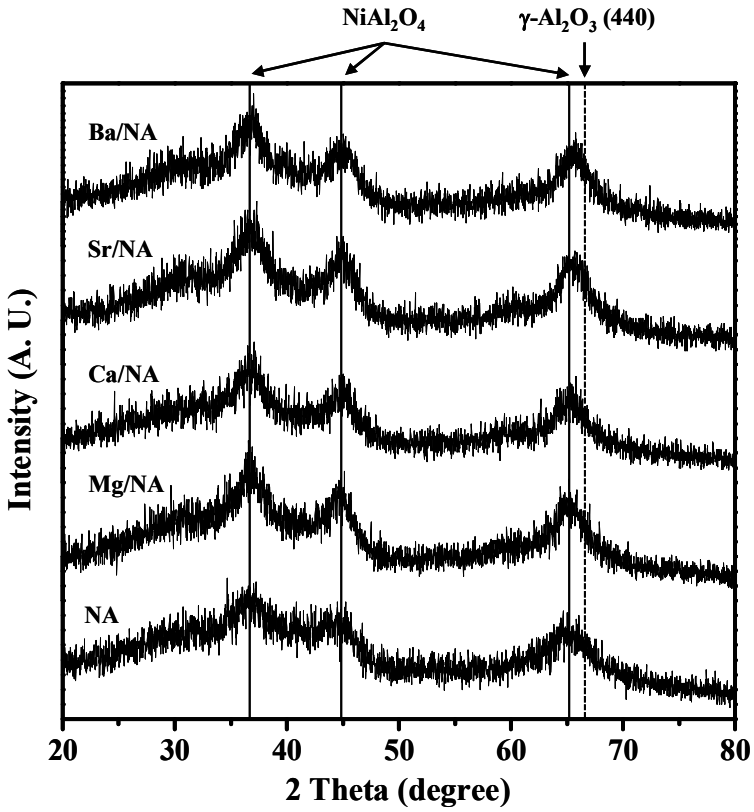

Fig. 3.2. XRD patterns of calcined NA and M/NA catalysts.

3.1.3. Reducibility and metal-support interaction

TPR measurements were carried out to examine the interaction between nickel species and alumina support in the NA and M/NA catalysts. Fig. 3.3 shows the TPR profiles of NA and M/NA (M = Mg, Ca, Sr, and Ba) catalysts calcined at 700 ^{o}C. No reduction band indicative of unsupported bulk nickel oxide was observed below 400 ^{o}C [31]. Instead, all the catalysts exhibited a single reduction band at around 700 ^{o}C, indicating the strong interaction between nickel species and alumina support through the formation of surface nickel aluminate phase [31-33]. This is well consistent with the XRD result (Fig. 3.2) showing the existence of nickel aluminate phase in both NA and M/NA catalysts. It has been reported that surface nickel aluminate phase has an intermediate reducibility between bulk nickel oxide and bulk nickel aluminate [33-35]. According to the previous studies [36,37], bulk nickel oxide is vulnerable to aggregation, and bulk nickel aluminate is hard to be reduced to active metallic nickel species. Therefore, it is expected that surface nickel aluminate phase with moderate metal-support interaction in the NA and M/NA catalysts has relatively high stability and reducibility. It was found that the reduction peak temperature of surface nickel aluminate phase in the M/NA catalysts was higher than that of NA catalyst. This means that the interaction between nickel species and alumina support in the M/NA catalysts was stronger than that in the NA catalyst.

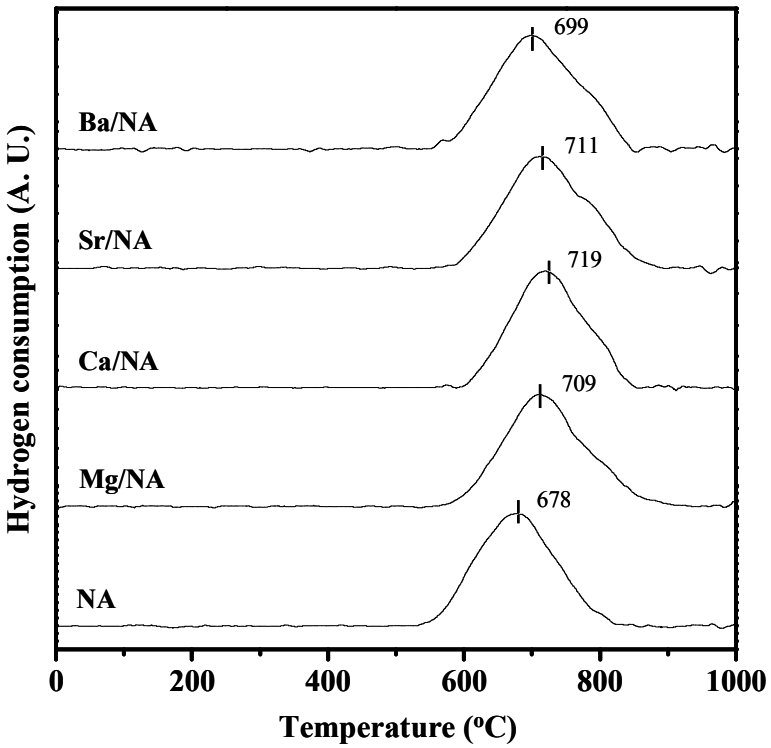

Fig. 3.3. TPR profiles of calcined NA and M/NA catalysts.

3.1.4. Characterization of reduced catalysts

XRD patterns of reduced NA and M/NA (M = Mg, Ca, Sr, and Ba) catalysts are presented in Fig. 3.4. It was observed that no diffraction peaks corresponding to nickel aluminate phase were detected in all the reduced catalysts. Instead, all the reduced catalysts showed the diffraction peaks indicative of metallic nickel (solid lines in Fig. 3.4). Furthermore, the diffraction peak of γ-Al_2O_3 (440) phase (dashed line in Fig. 3.4) clearly appeared in all the reduced catalysts, when compared to the diffraction peak of the calcined catalysts (dashed line Fig. 3.2). This indicates that nickel species were excluded from γ-Al_2O_3 lattice during the reduction process, leading to lattice contraction of γ-Al_2O_3. That is, nickel aluminate phase in both NA and M/NA catalysts was successfully reduced into metallic nickel during the reduction process employed in this work.

Hydrogen chemisorption measurements were conducted in order to determine the nickel surface area, nickel dispersion, and average nickel diameter in the reduced NA and M/NA (M = Mg, Ca, Sr, and Ba) catalysts. Hydrogen chemisorption results for reduced NA and M/NA catalysts are listed in Table 3.2. Nickel surface area of the reduced catalysts decreased in the order of Mg/NA > Sr/NA > Ca/NA > NA > Ba/NA. As a consequence, nickel dispersion decreased in the order of Mg/NA > Sr/NA > Ca/NA > NA > Ba/NA, and average nickel diameter increased in the order of Mg/NA < Sr/NA < Ca/NA < NA < Ba/NA. Average nickel diameter in all the catalysts was less than 20 nm, implying strong resistance toward the aggregation of nickel

species. This was further confirmed by TEM images as presented in Fig. 3.5. No agglomerates of metallic nickel larger than 20 nm were found in the reduced NA (Fig. 3.5 (a)) and M/NA catalysts (Fig. 3.5 (b) and Fig. 3.5 (c)).

According to the previous studies [38-40], alkaline earth metal doped on Ni-based catalysts increases nickel surface area and nickel dispersion by acting as a spacer. Especially, magnesium-promoted nickel catalyst is known to retain NiO-MgO solid solution, because NiO and MgO have a face-centered cubic structure as well as similar size of lattice parameter [41]. This additional strong interaction between NiO and MgO inhibits nickel sintering during the reduction process. However, Ba/NA catalyst showed smaller nickel surface area than NA catalyst. Ba retains larger atomic radius than the other alkaline earth metals, which inhibits the incorporation of Ba atoms into the crystalline structure of nickel-alumina catalyst. This results in coverage of active nickel sites by Ba atoms on the surface of Ba/NA catalyst, as similarly observed for lanthanum-doped Ni catalyst [42,43].

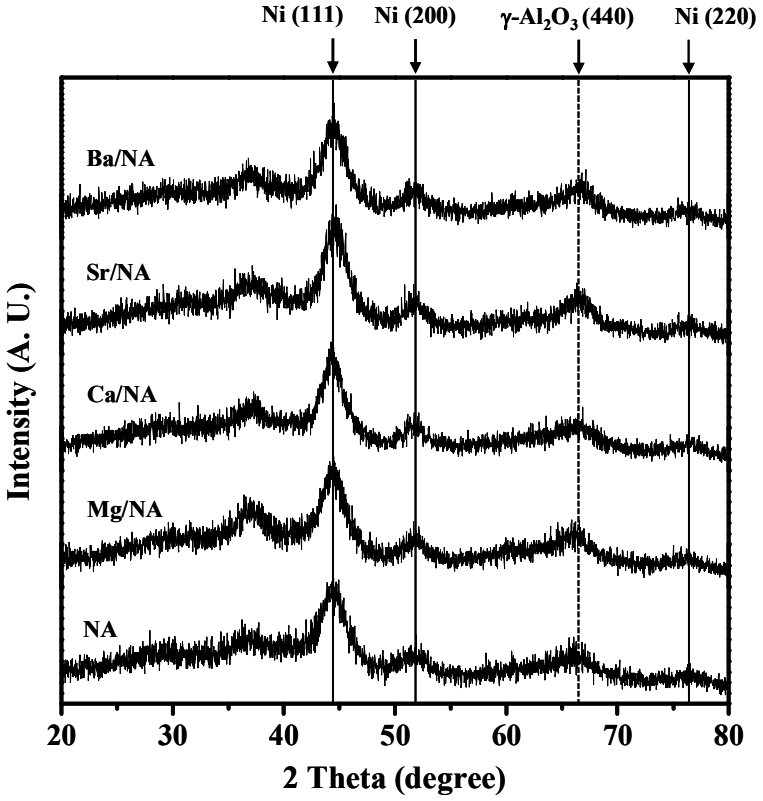

Fig. 3.4. XRD patterns of reduced NA and M/NA catalysts.

Table 3.2

Hydrogen chemisorption results for reduced NA and M/NA catalysts

Catalyst	Nickel surface area (m^2/g-Ni) [a]	Nickel dispersion (%)[a]	Average nickel diameter (nm)[a]
NA	39.2	5.9	17.2
Mg/NA	43.9	6.6	15.3
Ca/NA	40.2	6.0	16.8
Sr/NA	40.6	6.1	16.6
Ba/NA	38.1	5.7	17.7

[a] Calculated by assuming $H/Ni_{atom} = 1$

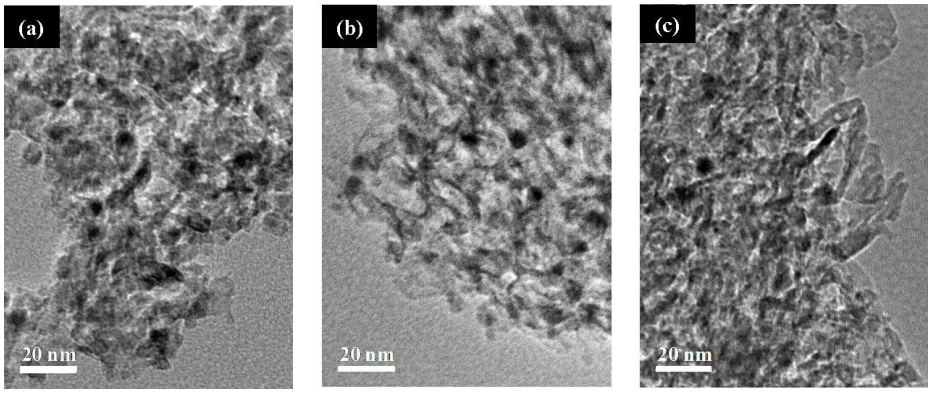

Fig. 3.5. TEM images of reduced (a) NA, (b) Mg/NA, and (c) Ba/NA catalysts.

3.1.5. Catalytic performance in the steam reforming of natural gas

Fig. 3.6 shows the natural gas conversion and hydrogen yield with time on stream in the steam reforming of natural gas over NA and M/NA (M = Mg, Ca, Sr, and Ba) catalysts at 600 ^{o}C. It was found that both NA and M/NA catalysts showed a stable catalytic performance without catalyst deactivation during the steam reforming reaction. The stable catalytic performance of both catalysts might be due to well-developed mesopores of the catalysts. It is believed that high surface area, large pore volume, and large average pore diameter of NA and M/NA catalysts played an important role in facilitating internal mass transfer of reactants and products during the reaction. Finely dispersed metallic nickel with a size less than 20 nm was also responsible for stable catalytic performance of NA and M/NA catalysts by suppressing carbon deposition and nickel sintering during the reaction [44].

However, the catalytic performance of M/NA catalysts was strongly affected by the identity of promoter. Both natural gas conversion and hydrogen yield decreased in the order of Mg/NA > Sr/NA > Ca/NA > NA > Ba/NA. Among the catalysts tested, Mg/NA catalyst exhibited the best catalytic performance in terms of natural gas conversion and hydrogen yield.

Fig. 3.7 shows the correlations between nickel surface area and catalytic performance of NA and M/NA catalysts in the steam reforming of natural gas. It is interesting to note that both natural gas conversion and hydrogen yield increased with increasing nickel surface area. This indicates that nickel surface area played an important role in determining the catalytic performance

of nickel-alumina xerogel catalysts in the steam reforming natural gas. According to the previous study [44], more active sites for C-H bond cleavage of methane are formed with increasing nickel surface area of nickel-based catalysts. In particular, high nickel surface area with small nickel particle size leads to the increase in the number of step sites of nickel catalysts, where dehydrogenation process preferentially occurs [45]. It is known that the dehydrogenation process is the rate-determining step in the steam reforming reaction [46,47]. Thus, nickel surface area served as a key factor determining the catalytic performance in the steam reforming of natural gas.

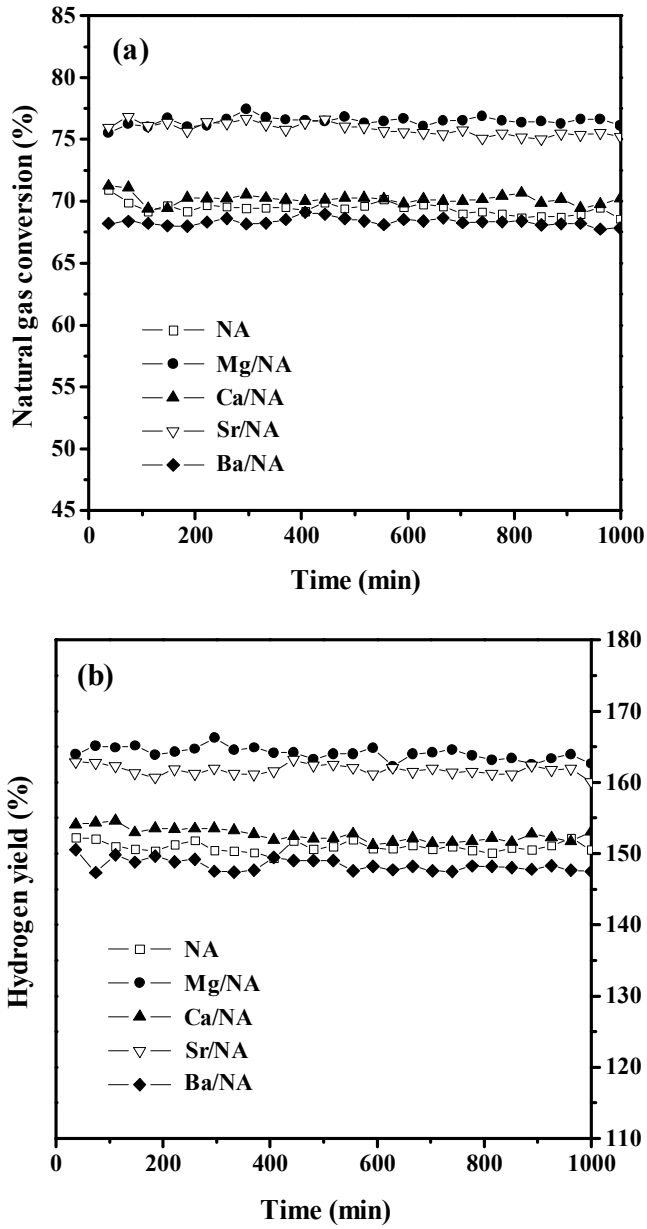

Fig. 3.6. (a) Natural gas conversion and (b) hydrogen yield with time on stream in the steam reforming of natural gas over NA and M/NA catalysts.

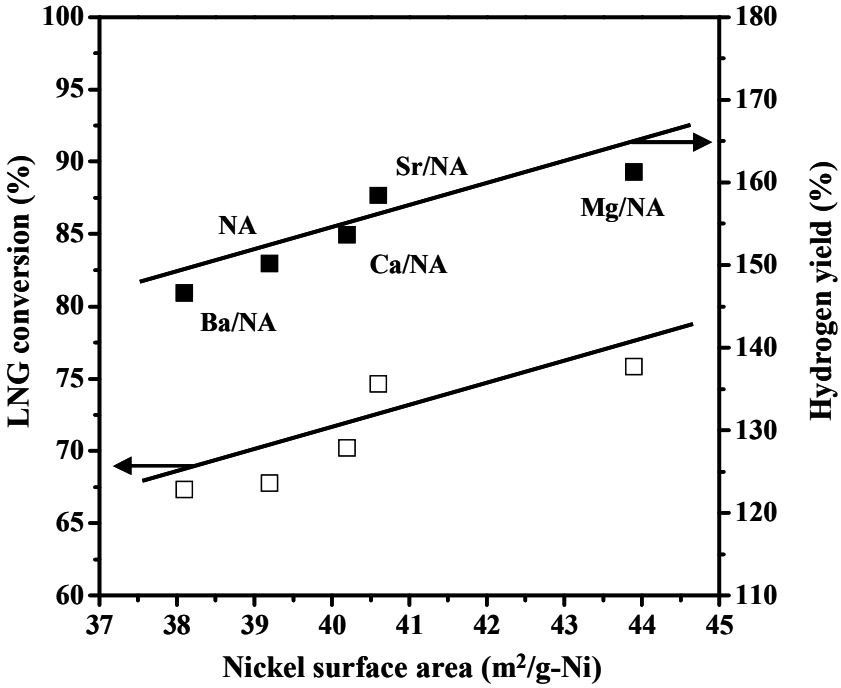

Fig. 3.7. Correlations between nickel surface area and catalytic performance of NA and M/NA catalysts in the steam reforming of natural gas. Catalytic performance data were obtained after a 1000 min-reaction at 600 °C.

3.1.6. Characterization of used catalysts

Table 3.3 shows the amount of carbon deposition on the used NA and M/NA catalysts after a 1000 min-reaction. The amount of carbon deposition on the NA catalyst was larger than that on the M/NA catalysts. Furthermore, the amount of carbon decreased in the order of NA > Mg/NA > Ca/NA ≈ Sr/NA > Ba/NA. This result might be related to the basic properties of the catalysts. It is known that acid sites are responsible for carbon deposition in the alumina supported catalysts [48,49]. In addition, introducing materials with high base strength into reforming catalysts is an effective way to reduce acidity of the catalysts. As base strength of alkaline earth metals increases with increasing atomic number [50,51], acidity of the catalysts is expected to decrease in the order of NA > Mg/NA > Ca/NA > Sr/NA > Ba/NA. This trend is well consistent with the trend of carbon deposition, as similarly reported in the previous study [52]. Thus, the introduction of alkaline earth metal with high atomic number into nickel-alumina xerogel catalysts was effective to suppress the carbon deposition.

Table 3.3

Amount of carbon deposition on the used catalysts after a 1000 min-reaction

Catalyst	NA	Mg/NA	Ca/NA	Sr/NA	Ba/NA
Amount of carbon deposition (wt%)[a]	3.1	1.4	0.5	0.5	0.3

[a] Determined by CHNS elemental analyses

3.2. Mesoporous nickel-alumina aerogel catalyst by a supercritical CO_2 drying method

3.2.1. Textural properties of calcined catalysts

Fig. 3.8 shows the nitrogen adsorption-desorption isotherms of calcined Mg/NAA and Mg/NAX catalysts. Both catalysts showed type-IV isotherms, indicating capillary condensation of well-developed mesoporous structure. It should be noted that Mg/NAA catalyst exhibited H1 type hysteresis due to its mesoporous structure formed by spherical agglomerates [53]. On the other hand, Mg/NAX catalyst showed H2 type hysteresis due to its "ink-bottle" type pores [26].

Detailed physicochemical properties of calcined Mg/NAA and Mg/NAX catalysts are summarized in Table 3.4. Both catalysts showed excellent textural properties with mesoporous structure even after high temperature calcination process (700 ^{o}C for 5 h). Ni loading and Mg loading of both catalysts were in good agreement with the designed values. These results suggest that both catalysts were successfully prepared in this work. However, Mg/NAA catalyst exhibited higher surface area, larger pore volume, and larger average pore diameter than Mg/NAX catalyst. It is known that metal framework is easy to be broken by mechanical power of surface tension when liquid in pores evaporates into gas phase at conventional drying condition [54]. This surface tension can be minimized when pore liquid changes into gas through supercritical condition [55]. Therefore, it can be

inferred that supercritical CO_2 drying method played an crucial role in maintaining gel structure and in enhancing textural properties of Mg/NAA catalyst during the preparation process.

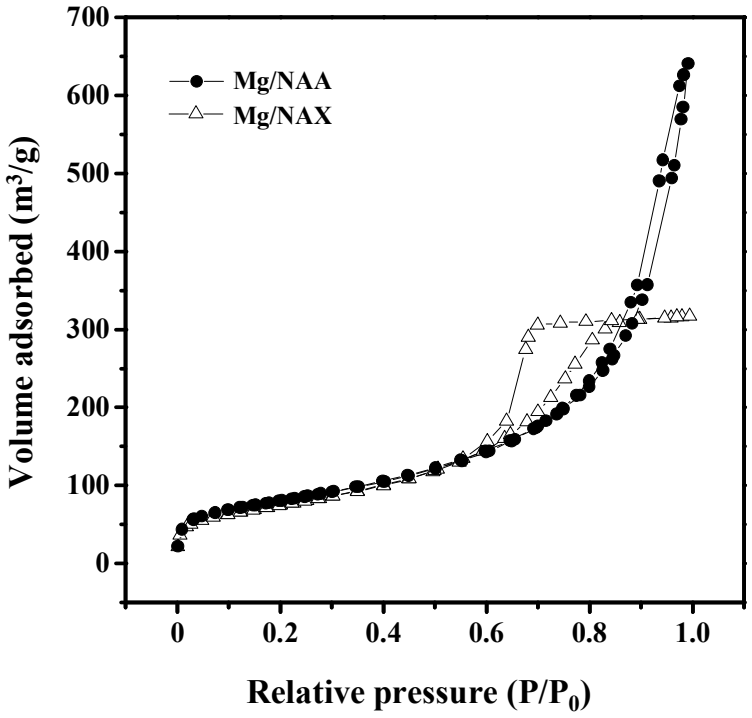

Fig. 3.8. Nitrogen adsorption-desorption isotherms of calcined Mg/NAA and Mg/NAX catalysts.

Table 3.4

Physicochemical properties of calcined Mg/NAA and Mg/NAX catalysts

Catalyst	Mg/NAA	Mg/NAX
Ni loading (wt%)[a]	20.6	21.1
Mg loading (wt%)[a]	2.0	1.9
Surface area (m^2/g)[b]	287	270
Pore volume (cm^3/g)[c]	0.98	0.49
Average pore diameter (nm)	13.7	7.3

[a] Determined by ICP-AES measurement
[b] Calculated by the BET equation
[c] Total pore volume at $P/P_0 \sim 0.990$

3.2.2. Crystalline structure of calcined catalysts

XRD patterns of Mg/NAA and Mg/NAX catalysts calcined at 700 ^{o}C for 5 h are shown in Fig. 3.9. It was found that diffraction peaks corresponding to bulk nickel oxide phase were not detected in the XRD patterns of both catalysts. Instead, both catalysts exhibited three diffraction peaks indicative of surface nickel aluminate phase (solid lines in Fig. 3.9). This means that nickel species were well incorporated into alumina lattice during condensation process by forming Ni-O-Al composite structure [56]. It is noteworthy that intensity of diffraction peaks for Mg/NAA catalyst was weaker than that for Mg/NAX catalyst. This means that nickel species in the Mg/NAA catalyst were more finely dispersed on alumina support than those in the Mg/NAX catalyst.

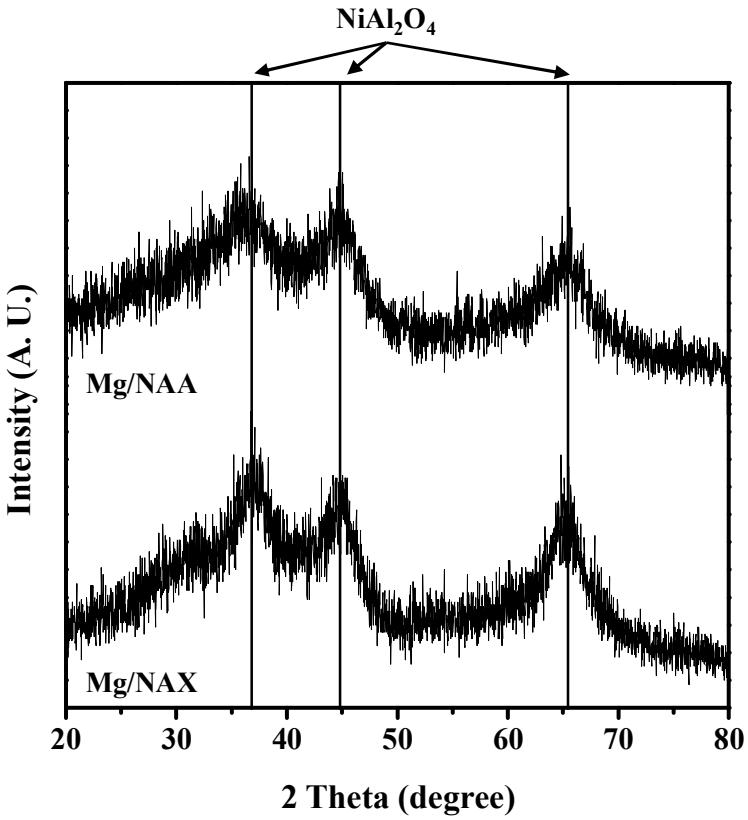

Fig. 3.9. XRD patterns of calcined Mg/NAA and Mg/NAX catalysts.

3.2.3. Reducibility and metal-support interaction

TPR measurements were conducted to investigate metal-support interaction in the Mg/NAA and Mg/NAX catalysts. Fig. 3.10 shows the TPR profiles of Mg/NAA and Mg/NAX catalysts calcined at 700 ^{o}C. Both catalysts showed a single reduction band at around 700 ^{o}C, corresponding to surface nickel aluminate phase [31], which is in good agreement with XRD results of calcined catalysts (Fig. 3.9). It is found that Mg/NAA catalyst showed higher reduction peak temperature than Mg/NAX catalyst. In other words, nickel species in the Mg/NAA catalyst more strongly interacted with alumina support than those in the Mg/NAX catalyst, although chemical compositions of both catalysts were nearly identical. This is because nickel species in the Mg/NAA catalyst were more finely dispersed than those in the Mg/NAX catalyst due to high surface area and large pore volume of Mg/NAA catalyst.

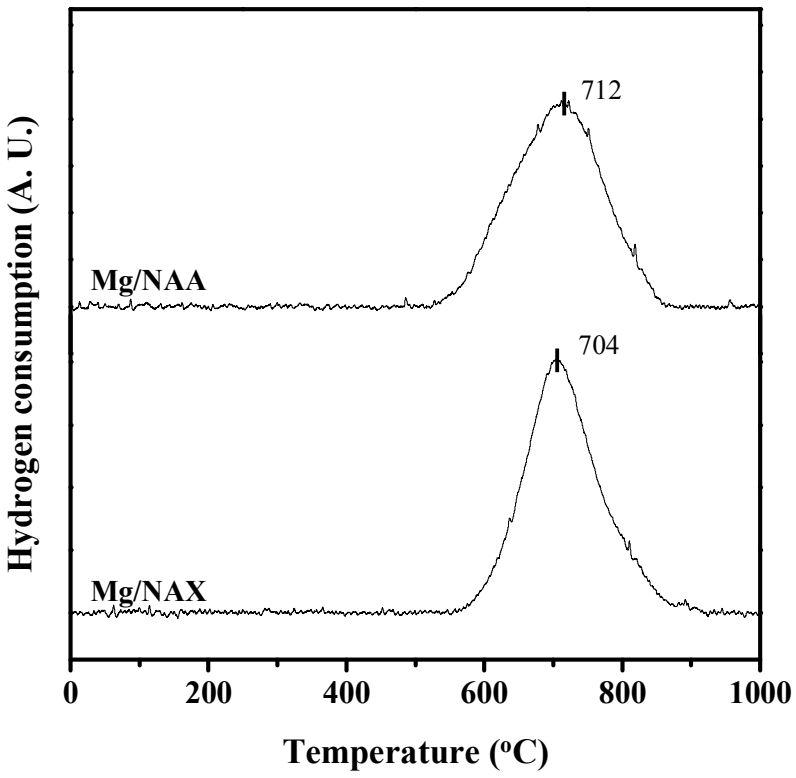

Fig. 3.10. TPR profiles of calcined Mg/NAA and Mg/NAX catalysts.

3.2.4. Characterization of reduced catalysts

Fig. 3.11 shows the XRD patterns of reduced Mg/NAA and Mg/NAX catalysts. It was observed that diffraction peaks indicative of surface nickel aluminate phase disappeared. Instead, both catalysts exhibited diffraction peaks corresponding to metallic nickel phase (solid lines in Fig. 3.11). This result indicates that nickel aluminate phase in both catalysts were completely reduced into metallic nickel phase during the reduction process employed in this work. It should be noted that Mg/NAA catalyst showed weaker intensities of diffraction peaks than Mg/NAX catalyst. This means that metallic nickel particles in the reduced Mg/NAA catalyst were smaller than those in the reduced Mg/NAX catalyst.

TEM analyses were performed to confirm nickel dispersion of Mg/NAA and Mg/NAX catalysts. Fig. 3.12 shows the TEM images of Mg/NAA (Fig. 3.12 (a)) and Mg/NAX (Fig. 3.12 (b)) catalysts reduced at 700 ^{o}C for 3 h. No large agglomerates of metallic nickel were found in the reduced Mg/NAA catalyst. On the other hand, Mg/NAX catalyst showed large aggregates of metallic nickel, representing relatively poor dispersion of metallic nickel in the Mg/NAX catalyst.

Hydrogen chemisorption measurements were conducted in order to determine nickel surface area, average nickel diameter, and nickel dispersion of the reduced Mg/NAA and Mg/NAX catalysts as listed in Table 3.5. Nickel surface area of Mg/NAA catalyst was larger than that of Mg/NAX catalyst. As a consequence, Mg/NAA catalyst showed smaller average nickel diameter and

higher nickel dispersion than Mg/NAX catalyst. This result implies that Mg/NAA catalyst retains more active nickel sites for catalytic reaction than Mg/NAX catalyst. This result is well consistent with XRD and TEM results. Therefore, it can be summarized that supercritical CO_2 drying employed for the preparation of Mg/NAA catalyst was essential for enhancing textural properties and nickel dispersion of Mg/NAA catalyst.

In order to investigate methane adsorption capacity, CH_4-TPD measurements were conducted (Fig. 3.13). Both catalyst exhibited a single desorption band at around 330 ^oC. According to the literature [26], carbon species desorbed at 300-400 ^oC are attributed to partially dehydrogenated carbon during the adsorption step. That is, a nickel catalyst which shows larger methane adsorption capacity in the CH_4-TPD measurement is expected to dissociate C-H bond more effectively in the reforming reactions. It is also known that C-H bond dissociation in the methane dehydrogenation process is the rate determining step of reforming reactions [45-47]. Therefore, methane adsorption capacity serves as a crucial factor determining the catalytic performance in the tri-reforming of methane.

The amount of desorbed methane was calculated from the peak area in the CH_4-TPD profiles as summarized in Table 3.6. It was observed that Mg/NAA catalyst showed larger amount of desorbed methane than Mg/NAX catalyst. According to the literature [44], methane adsorption site of nickel catalyst, which is active for dissociating C-H bond of methane, increases with increasing nickel dispersion of the catalyst. Therefore, Mg/NAA catalyst with high nickel dispersion showed high methane adsorption capacity. Thus, it is expected that Mg/NAA catalyst with higher nickel dispersion and larger

methane adsorption capacity would show higher catalytic activity than Mg/NAX catalyst in the steam reforming of natural gas.

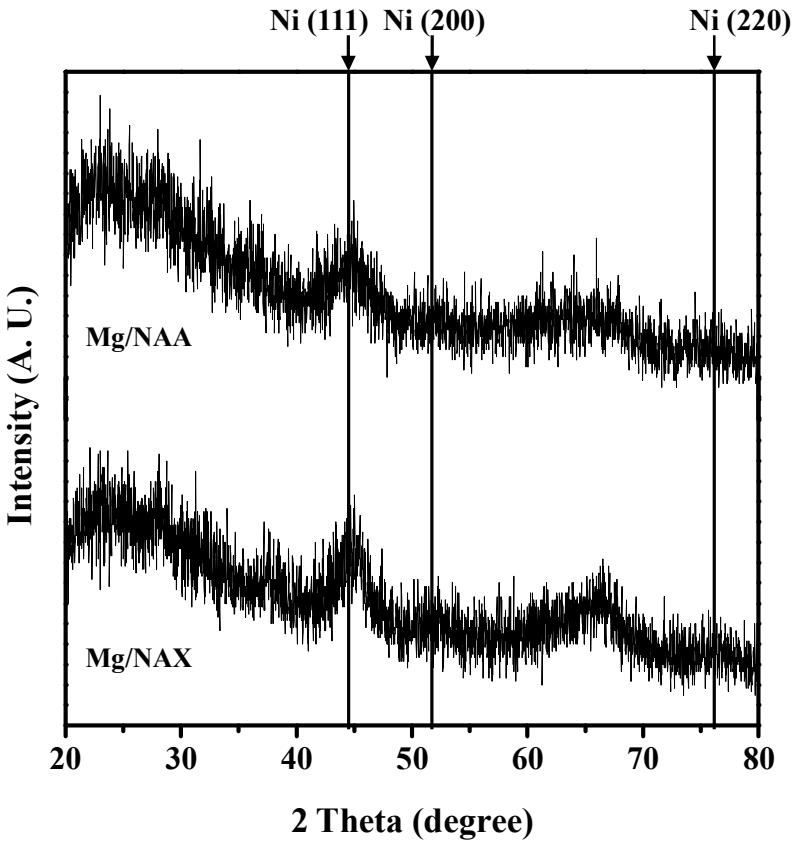

Fig. 3.11. XRD patterns of reduced Mg/NAA and Mg/NAX catalysts.

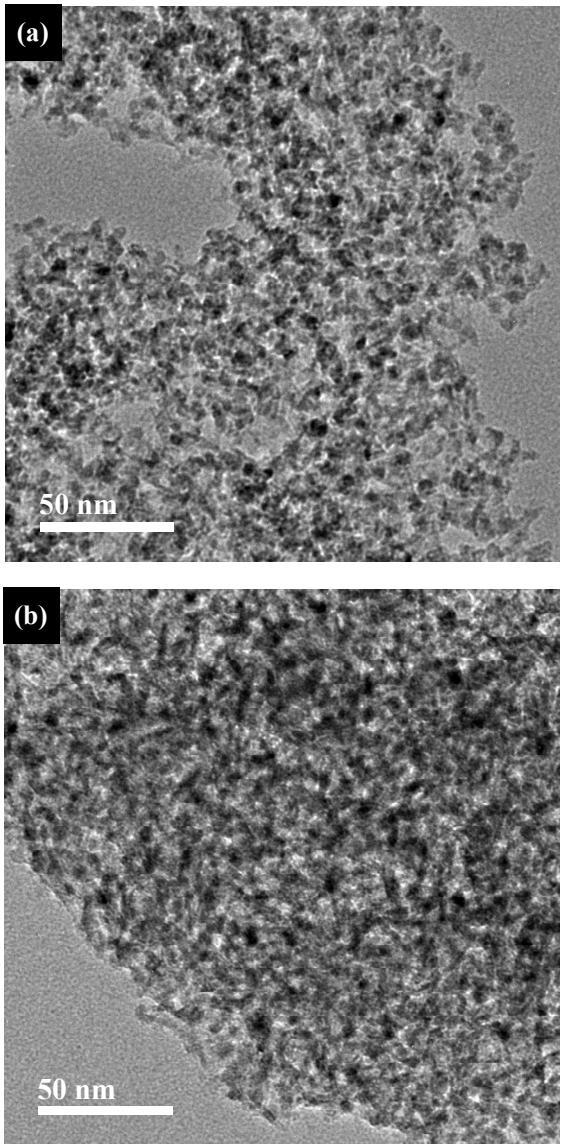

Fig. 3.12. TEM images of reduced (a) Mg/NAA and (b) Mg/NAX catalysts.

Table 3.5

Hydrogen chemisorption results for reduced Mg/NAA and Mg/NAX catalysts

Catalyst	Nickel surface area (m^2/g-Ni) [a]	Nickel dispersion (%)[a]	Average nickel diameter (nm)[a]
Mg/NAA	51.2	7.7	13.2
Mg/NAX	38.9	6.5	17.3

[a] Calculated by assuming $H/Ni_{atom} = 1$

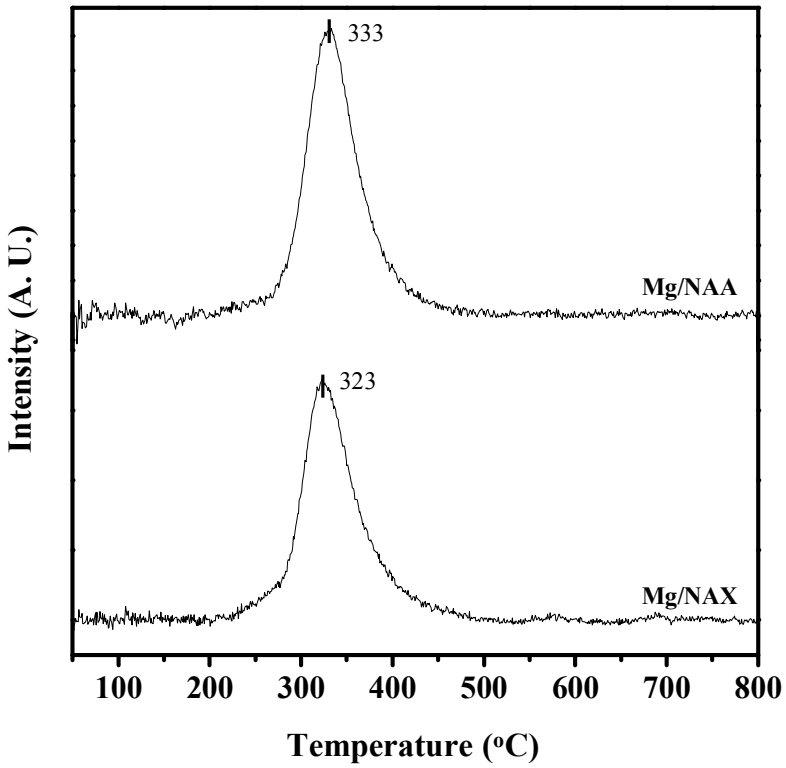

Fig. 3.13. CH_4-TPD profiles of reduced Mg/NAA and (b) Mg/NAX catalysts.

Table 3.6

Amount of desorbed CH_4 on reduced Mg/NAA and Mg/NAX catalysts

Catalyst	Mg/NAA	Mg/NAX
Amount of desorbed CH_4 (μmol-CH_4/g)	45.3	38.4

3.2.5. Catalytic performance in the steam reforming of natural gas

Fig. 3.14 shows the catalytic performance of Mg/NAA and Mg/NAX catalysts in the steam reforming of natural gas at 600 ^{o}C. Both catalysts showed a stable catalytic activity without noticeable deactivation during a 1000-min reaction. It is believed that well-developed mesoporous structure and finely dispersed nickel species of Mg/NAA and Mg/NAX catalysts suppressed nickel sintering and carbon deposition. However, Mg/NAA catalyst showed higher hydrogen yield and higher natural gas conversion than Mg/NAX catalyst. According to the previous study [47], cleavage of C-H bonds in methane molecule is the rate determining step of steam reforming reaction. Therefore, a nickel catalyst with high nickel dispersion, which contains large amount of active nickel sites to dissociate C-H bonds, is expected to exhibit high catalytic activity in the steam reforming process. Therefore, it is concluded that high nickel dispersion of Mg/NAA catalyst served as a key factor for its high catalytic performance in the hydrogen production by steam reforming of natural gas.

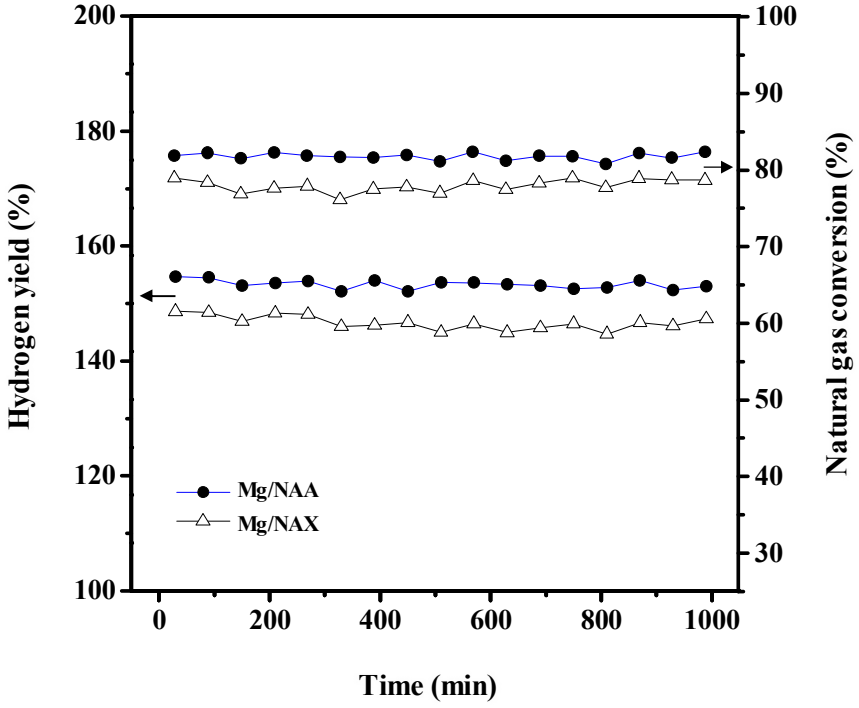

Fig. 3.14. Natural gas conversion and hydrogen yield with time on stream in the steam reforming of natural gas over Mg/NAA and Mg/NAX catalysts.

3.3. Mesoporous vanadium-nickel-alumina xerogel catalyst

3.3.1. Textural properties of calcined catalysts

Textural properties of calcined xVNA catalysts are shown in Fig. 3.15. All the catalysts showed type IV isotherms according to the international union of pure and applied chemistry (IUPAC) classification, indicating mesoporous characteristics of the samples with interconnected pore geometry and a high energy of adsorption [57]. In addition, all the catalysts exhibited high surface area, large pore volume, and large pore diameter, as listed in Table 3.7. This result indicates that all the xVNA catalysts were successfully prepared by an epoxide-driven sol-gel method to have well-developed mesopores [58]. The excellent textural properties of calcined xVNA catalysts are expected to provide an opportunity for active metal species to be highly dispersed [57].

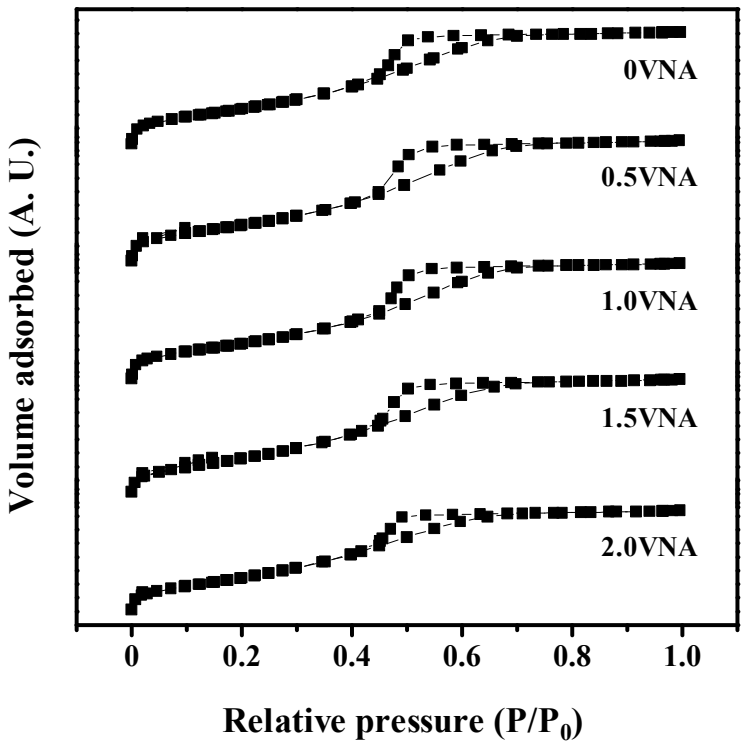

Fig. 3.15. Nitrogen adsorption-desorption isotherms of calcined xVNA catalysts.

Table 3.7

Textural properties of calcined xVNA catalysts

Catalyst	Surface area (m^2/g)[a]	Pore volume (cm^3/g)[b]	Average pore diameter (nm)
0VNA	323	0.35	4.4
0.5VNA	328	0.38	4.6
1.0VNA	320	0.36	4.5
1.5VNA	343	0.37	4.3
2.0VNA	330	0.33	4.0

[a] Calculated by the BET equation
[b] Total pore volume at $P/P_0 \sim 0.990$

3.3.2. Crystalline structure of calcined catalysts

Fig. 3.16 shows the X-ray diffractograms of calcined xVNA catalysts. The crystalline phases were identified by the JCPDS standards. The peaks at 2θ = 37.0°, 45.0°, and 65.5° observed in all the diffraction patterns were attributed to $NiAl_2O_4$ (JCPDS 10-0339) phase. This result indicates that $NiAl_2O_4$ spinel phase was formed during the calcination step at 700 °C. The formation of $NiAl_2O_4$ crystallite phase is known to take place by insertion of Ni^{2+} ions into the tetrahedral vacancies of γ-Al_2O_3 lattice [58]. It should be noted that broad and poorly defined peaks represent low crystallinity of xVNA catalysts, indicating fine dispersion of nickel species on γ-Al_2O_3 support [59].

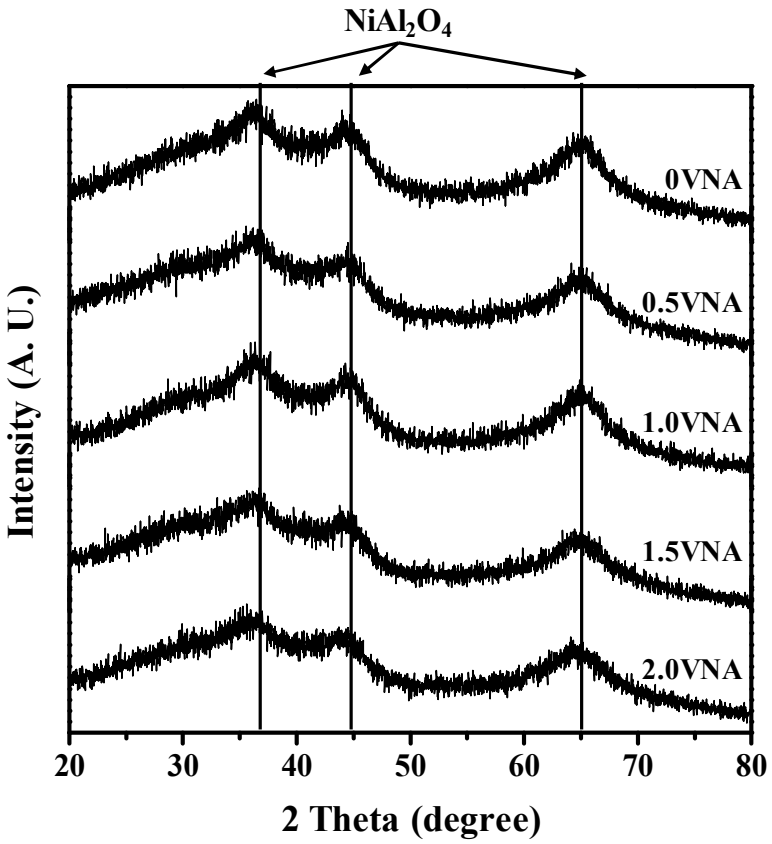

Fig. 3.16. XRD patterns of calcined xVNA catalysts.

3.3.3. Reducibility and metal-support interaction

TPR profiles of calcined xVNA catalysts are presented in Fig. 3.17. Main broad peak of xVNA catalysts was observed at around 600-700 ^{o}C. This dominant peak originates from the reduction of highly dispersed surface nickel aluminate spinel ($NiAl_2O_4$) in the xVNA catalysts [60]. It is interesting to note that the peak temperature of vanadium-free 0VNA catalyst was highest, while vanadium-containing nickel-alumina catalysts showed a peak shift to lower temperature. According to the previous research, vanadium species added to nickel-alumina catalysts make alloy with nickel species, resulting in the modification of electronic properties of nickel [31]. It was reported that nickel species in the vanadium-containing catalysts received electrons from vanadium, making nickel species more reducible.

Apart from the main broad peak, xVNA (x = 1.0, 1.5, and 2.0) catalysts showed an additional minor reduction peak at low temperature, which was attributed to the reduction of bulk nickel oxide to Ni^0 [61]. It is believed that the addition of vanadium higher than a certain level inhibited the interaction between nickel and alumina support, forming a bulk phase of nickel species. However, no characteristic peak indicative of vanadium reduction was observed because of very small amount of vanadium in the xVNA catalysts. It should be noted that the pre-reduction step for steam reforming reaction was carried out at 700 °C (Section 2.3). This temperature was higher than the reduction peak temperature of xVNA catalysts (Fig. 3.17). Therefore, it is believed that the reduction condition of this work was sufficient to completely

reduce nickel species into metallic nickel.

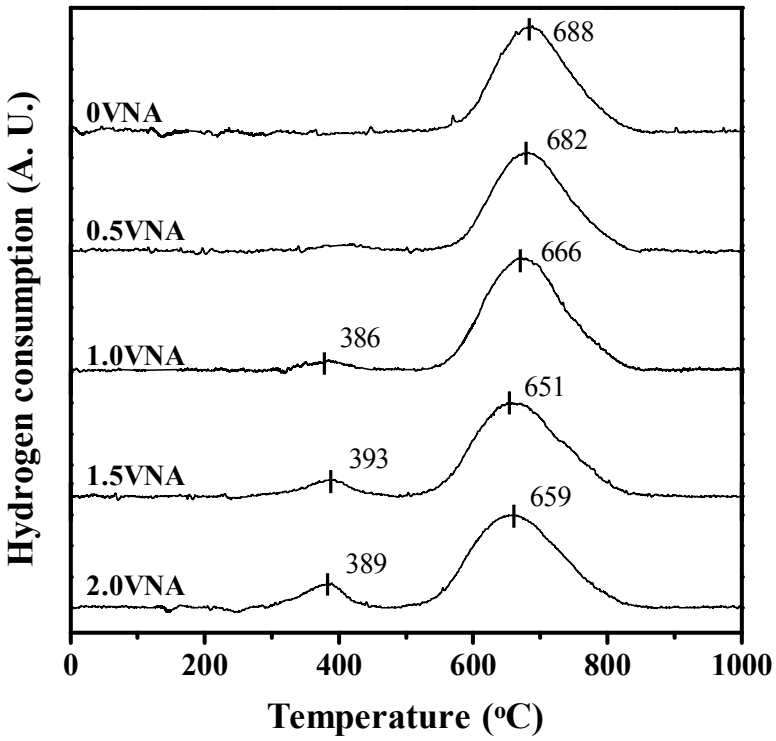

Fig. 3.17. TPR profiles of calcined xVNA catalysts.

3.3.4. Characterization of reduced catalysts

XRD patterns of reduced xVNA catalysts are presented in Fig. 3.18. No obvious characteristic peaks of nickel aluminate phase were observed. Instead, all the catalysts showed diffraction peaks at 2θ = 44.5°, 51.8°, and 76.4°, which were attributed to metallic nickel (JCPDS 04-0850) phase. Thus, nickel species in the xVNA catalysts were successfully reduced into metallic nickel during the reduction step employed in this work.

It was observed that intensities of diffraction peaks for reduced xVNA catalysts decreased as the vanadium loading increased up to 1.0 wt%. The intensities of diffraction peaks of xVNA catalysts then increased as the vanadium loading increased further. Average crystallite sizes of nickel particles were calculated by applying the Scherrer equation to the peak broadening of Ni (111) as summarized in Table 3.8. It was found that the amount of vanadium addition strongly affected the crystallite size of vanadium-nickel-alumina catalysts. According to the previous work, vanadium species exhibit high mobility on a catalyst surface because of its lower melting point than the reduction temperature [25]. As a result, highly mobile vanadium can inhibit the nickel mobility, suppressing the sintering of nickel particles. The increase of nickel crystallite size at high vanadium loading is believed to be due to the reduced dispersion effect caused by the formation of aggregated vanadium species [63].

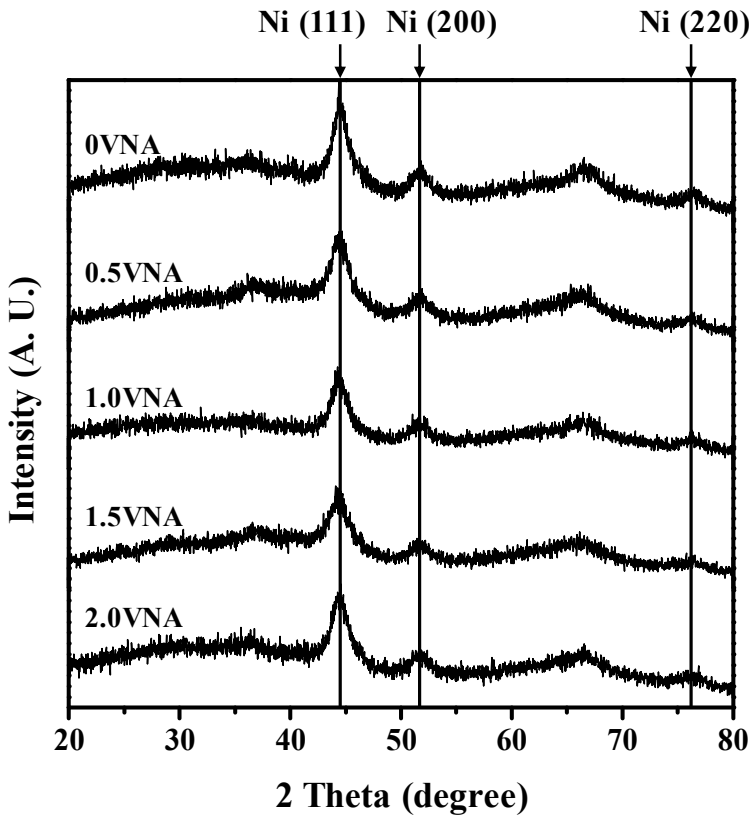

Fig. 3.18. XRD patterns of reduced xVNA catalysts.

Table 3.8

Crystallite size of metallic nickel in the reduced xVNA catalysts

Catalyst	0VNA	0.5VNA	1.0VNA	1.5VNA	2.0VNA
Crystallite size of metallic nickel (nm)[a]	5.4	4.7	4.6	4.6	4.9

[a] Calculated by the Scherrer equation from Ni (111) diffraction peak broadening in Fig. 3.18

3.3.5. Catalytic performance in the steam reforming of natural gas

Steam reforming of natural gas over reduced xVNA catalysts was carried out at 550 ^{o}C as presented in Fig. 3.19. Even at low reaction temperature, all the catalysts showed high catalytic performance in terms of natural gas conversion (> 50%) and hydrogen yield (> 100%). Furthermore, no significant deactivation was observed during the reaction. This is probably due to the fact that well-developed mesopores constructed by the sol-gel preparation method provided sufficient textural properties of xVNA catalysts, which facilitated internal diffusion of reactants and products during the reaction [64].

Fig. 3.20 shows the natural gas conversion and hydrogen yield over xVNA catalysts in the steam reforming of natural gas, plotted as a function of vanadium loading. The catalytic performance showed a volcano-shaped trend with respect to vanadium loading. Among the catalysts, 1.0VNA catalyst with an intermediate amount of vanadium loading exhibited the best catalytic performance. This is due to small nickel crystallite size of 1.0VNA catalyst. Small nickel crystallite in highly dispersed nickel-based catalysts usually contains high proportion of step sites. The step sites are known to facilitate dehydrogenation of methane and ethane, which is the rate-determining step of steam reforming reaction [21]. Thus, 1.0VNA catalyst with small nickel crystallite size showed high catalytic performance in the steam reforming of natural gas.

Fig. 3.21 shows the correlations between crystallite size of metallic

nickel and catalytic performance of xVNA catalysts. Natural gas conversion and hydrogen yield increased with decreasing nickel crystallite size. From the result, it is concluded that the addition of an appropriate amount of vanadium into nickel-alumina catalyst improved the catalytic performance in the steam reforming of natural gas by producing small-sized metallic nickel.

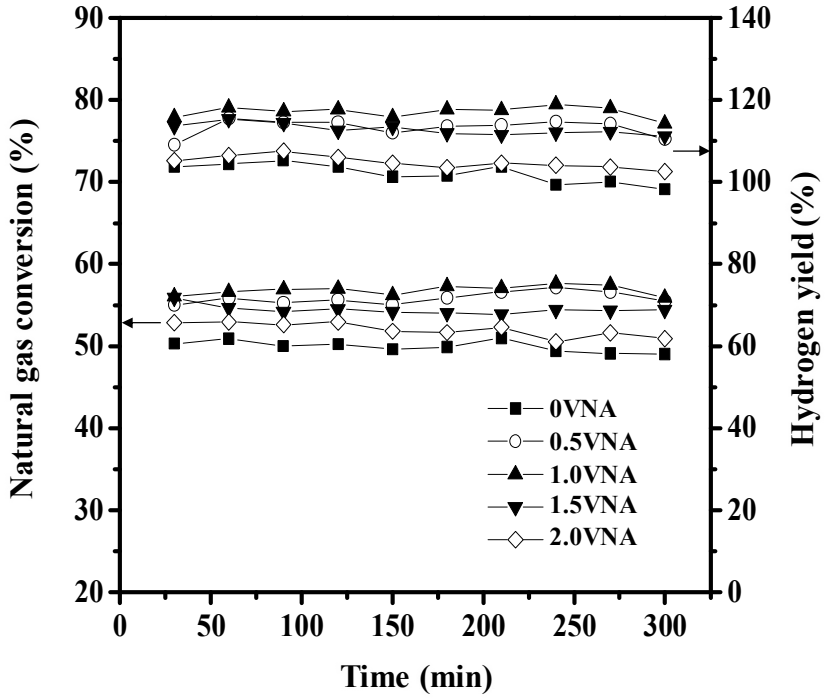

Fig. 3.19. Catalytic performance with time on stream in the steam reforming of natural gas over xVNA catalysts at 550 ^{o}C.

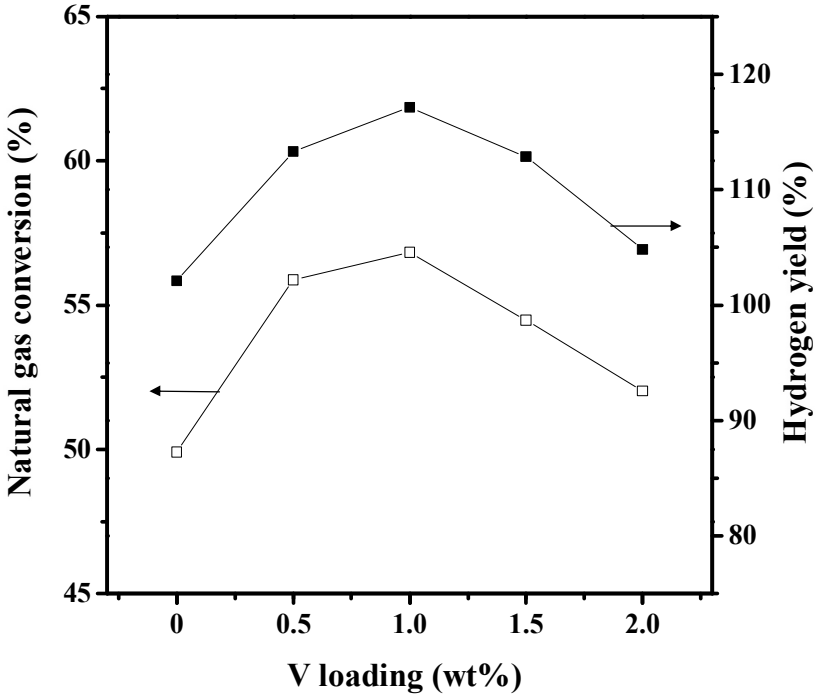

Fig. 3.20. Average catalytic performance plotted as a function of vanadium loading.

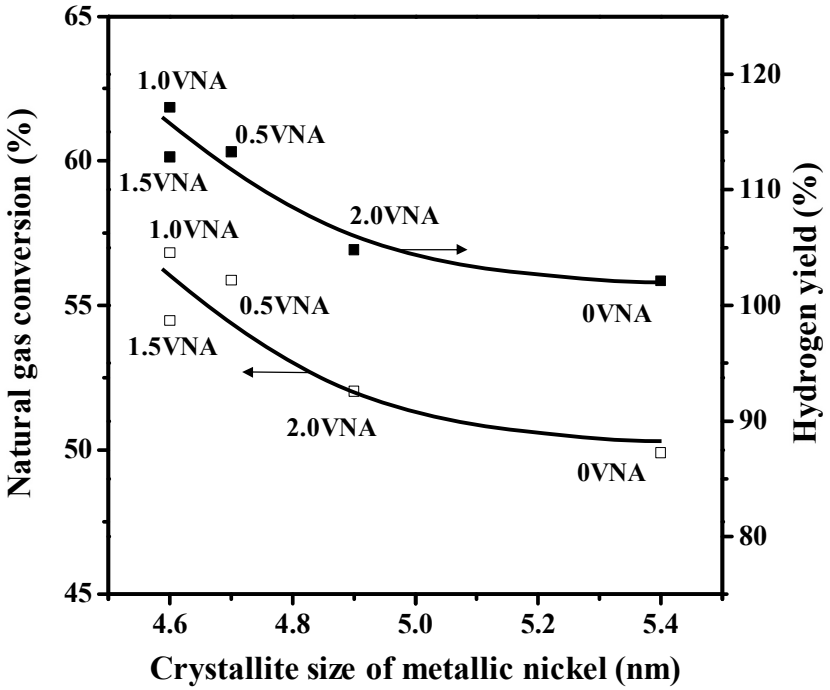

Fig. 3.21. Correlations between average catalytic performance and crystallite size of metallic nickel of xVNA catalysts.

3.4. Mesoporous nickel/alumina catalyst by a butyric acid-assisted impregnation method

3.4.1. Surface chemical state of as-prepared catalysts

In order to investigate chemical state of butyric acid, as-prepared xBAN/A (x = 0, 0.1, 0.25, 0.5, and 1) catalysts were examined by FT-IR analyses (Fig. 3.22). xBAN/A catalysts with butyric acid addition ($x \geq 0.25$) showed two small bands at 2975 cm^{-1} and 2885 cm^{-1}, which were indicative of asymmetric CH_2 stretch and symmetric CH_2 stretch, respectively [65]. The intensity of CH_2 stretch peaks increased with increasing butyric acid addition. Characteristic peaks indicative of asymmetric COO^- stretch (1565 cm^{-1}) and symmetric COO^- stretch (1465 cm^{-1}) were also detected in the catalysts with $x \geq 0.25$ [66]. According to the previous research [65], bonding types of COO^- groups to catalyst surface can be determined by the wavenumber separation ($\triangle$) between the asymmetric and the symmetric COO^- stretch. If $\triangle$ is large (> 200 cm^{-1}), monodentate interaction is expected. Small $\triangle$ (< 110 cm^{-1}) is for chelating bidentate mode. The medium range (140 cm^{-1} < $\triangle$ < 190 cm^{-1}) corresponds to bridging bidentate mode. In this work, $\triangle$ (1565 - 1465 = 100 cm^{-1}) was smaller than 110 cm^{-1}, indicating that butyric acid was bound to catalyst surface in a chelating bidentate mode. It should be noted that the peak at 1710 cm^{-1}, which was ascribed to C=O stretch of free butyric acid, appeared in the 1BAN/A catalyst [67]. This implies that butyric acid was

presented as a separated form on the catalyst surface, when excess amount of butyric acid was introduced.

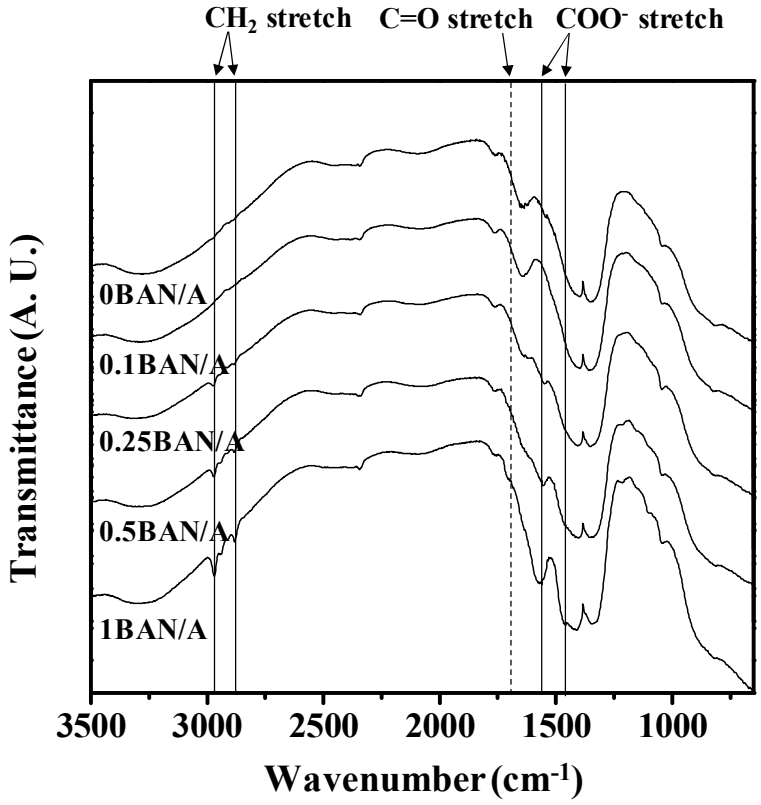

Fig. 3.22. FT-IR spectra of as-prepared xBAN/A catalysts.

3.4.2. Textural properties of calcined catalysts

Nitrogen adsorption-desorption isotherms of calcined xBAN/A catalysts are shown in Fig. 3.23. The obtained isotherms of all catalysts were type IV, indicating the formation of mesoporous structure [68]. In addition, H2-type hysteresis loops were observed for all catalysts, representing the existence of "ink-bottle" type pores [69]. Table 3.9 shows the detailed textural properties of xBAN/A catalysts. All the catalysts showed high surface area (> 250 m^2), large pore volume (> 0.5 cm^3/g), and large pore diameter (> 8.0 nm). This result means that the mesoporous structure of alumina support used for the preparation of xBAN/A catalysts was successfully prepared via a sol-gel method in this work [44].

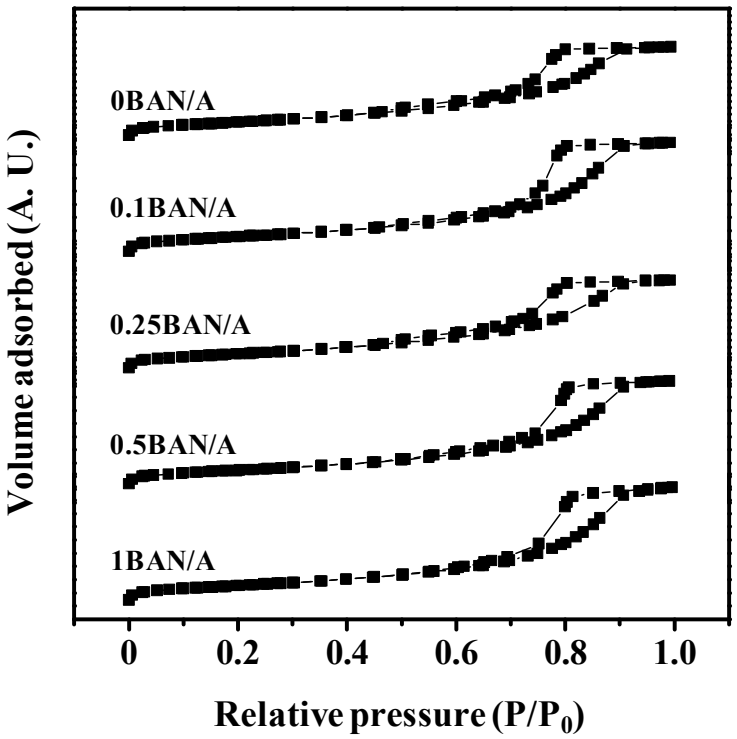

Fig. 3.23. Nitrogen adsorption-desorption isotherms of calcined xBAN/A catalysts.

Table 3.9

Textural properties of calcined xBAN/A catalysts

Catalyst	Surface area (m^2/g)[a]	Pore volume (cm^3/g)[b]	Average pore diameter (nm)
0BAN/A	257	0.55	8.5
0.1BAN/A	276	0.67	9.7
0.25BAN/A	265	0.55	8.3
0.5BAN/A	262	0.64	9.7
1BAN/A	274	0.69	10.1

[a] Calculated by the BET equation
[b] Total pore volume at $P/P_0 \sim 0.990$

3.4.3. Crystalline structure of calcined and reduced catalysts

X-ray diffractograms of calcined xBAN/A catalysts are presented in Fig. 3.24 (a). The crystalline phases were identified by the JCPDS standards. All the catalysts showed the characteristic diffraction peaks of nickel aluminate (JCPDS 10-0339) phase. This means that nickel aluminate spinel phase was formed during the calcination step. The formation of nickel aluminate phase is known to take place by the insertion of nickel cations into the tetrahedral vacancies of γ-Al_2O_3 lattice [70]. Accordingly, diffraction peak of γ-Al_2O_3 (440) slightly shifted to lower angle, indicating lattice expansion by the insertion of nickel species [71]. It is also noteworthy that broad and poorly defined peaks represent low crystallinity of xBAN/A catalysts, indicating fine dispersion of nickel species on γ-Al_2O_3 support [72].

Fig. 3.24 (b) shows the X-ray diffractograms of reduced xBAN/A catalysts. Diffraction peaks which were attributed to nickel aluminate phase disappeared. Instead, all the catalysts showed diffraction peaks ascribed to metallic nickel (JCPDS 04-0850) phase. Moreover, the diffraction peak indicative of γ-Al_2O_3 (440) shifted back to higher value, representing the exclusion of nickel cations from alumina lattice. Thus, it can be concluded that nickel species in the xBAN/A catalysts were sufficiently reduced from Ni^{2+} into Ni^0 during the reduction step.

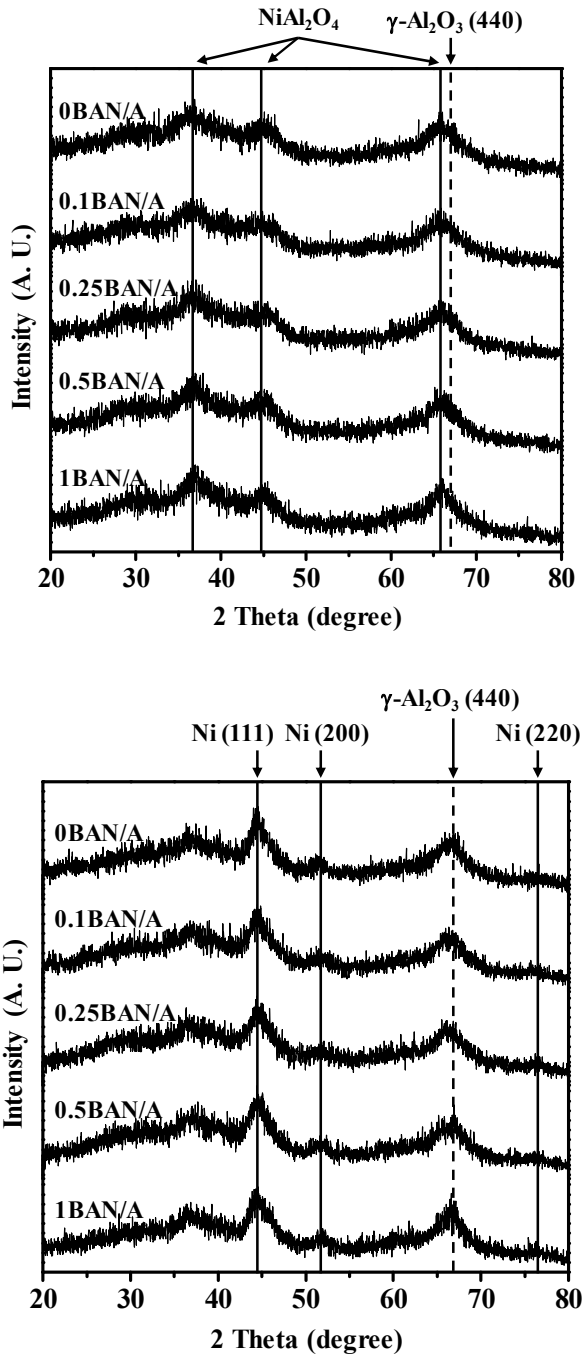

Fig. 3.24. XRD patterns of (a) calcined and (b) reduced xBAN/A catalysts.

3.4.4. Morphology of calcined and reduced catalysts

Distributions of aluminum, nickel, and oxygen in the calcined 0.25BAN/A catalyst were examined by SEM-EDS mapping analyses as shown in Fig. 3.25. The EDS elemental mapping image shows that nickel species (green dots in Fig. 3.25) was homogeneously dispersed on alumina support. TEM images of reduced 0.25BAN/A catalyst are shown in Fig. 3.26. It was estimated that crystallite size of nickel particle was smaller than 10 nm (Fig. 3.26 (a)). A large agglomerate of nickel particle was not observed in this sample. From the SEM-EDS and TEM results, it can be said that nickel species in the 0.25BAN/A catalyst was finely dispersed on alumina support. Fig. 3.26 (b) shows a lattice-resolved TEM image of the reduced 0.25BAN/A catalyst including inter-planar spacing of nickel crystallite. The periodic lattice fringe with a d-spacing of 0.20 ± 0.004 nm is attributed to the (111) plane of metallic nickel [73,74]. No lattice fringe indicative of nickel oxide phase was observed. Therefore, it is believed that the nickel species in the 0.25BAN/A catalyst was fully reduced into the metallic nickel phase during the reduction step. This result is in good agreement with the XRD results in Section 3.4.3.

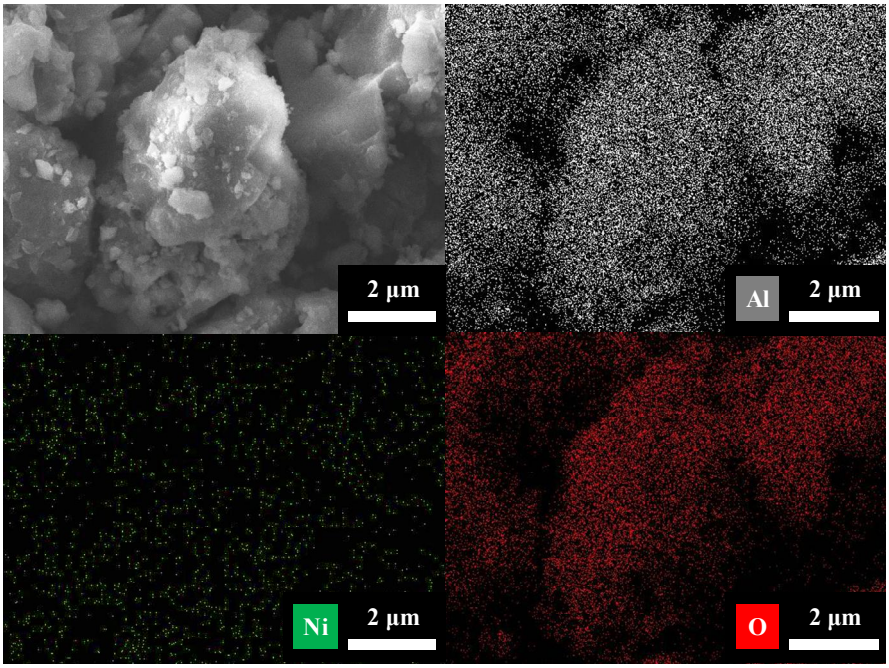

Fig. 3.25. SEM-EDS images of calcined 0.25BAN/A catalyst obtained by mapping on aluminum, nickel, and oxygen.

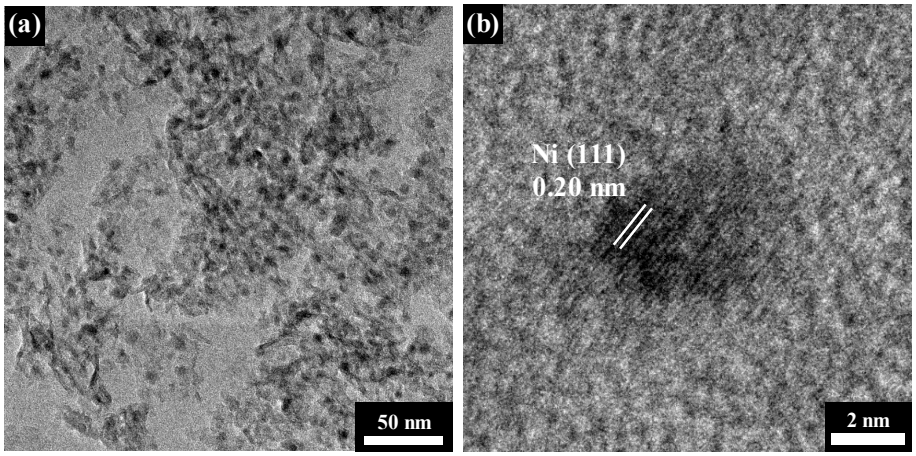

Fig. 3.26. TEM images of reduced 0.25BAN/A catalyst: (a) TEM image and (b) HR-TEM image with lattice fringes.

3.4.5. Reducibility and metal-support interaction

Fig. 3.27 shows the TPR profiles of calcined xBAN/A catalysts. All the xBAN/A catalysts showed a reduction peak at around 700 ^{o}C due to highly dispersed nickel aluminate spinel [31]. It was observed that the peak temperature of xBAN/A (x > 0) catalysts with butyric acid addition showed peak shift to low temperature compared to 0BAN/A catalyst. It can be inferred that butyric acid weakened the interaction between metal and support by surrounding metal particles. In particular, 1BAN/A catalyst showed an additional reduction peak at 489 ^{o}C, indicating the reduction of bulk nickel oxide to metallic nickel [62]. It is believed that the excessively added butyric acid surrounding nickel species lifts up the nickel cluster from alumina, inhibiting the interaction between nickel and alumina.

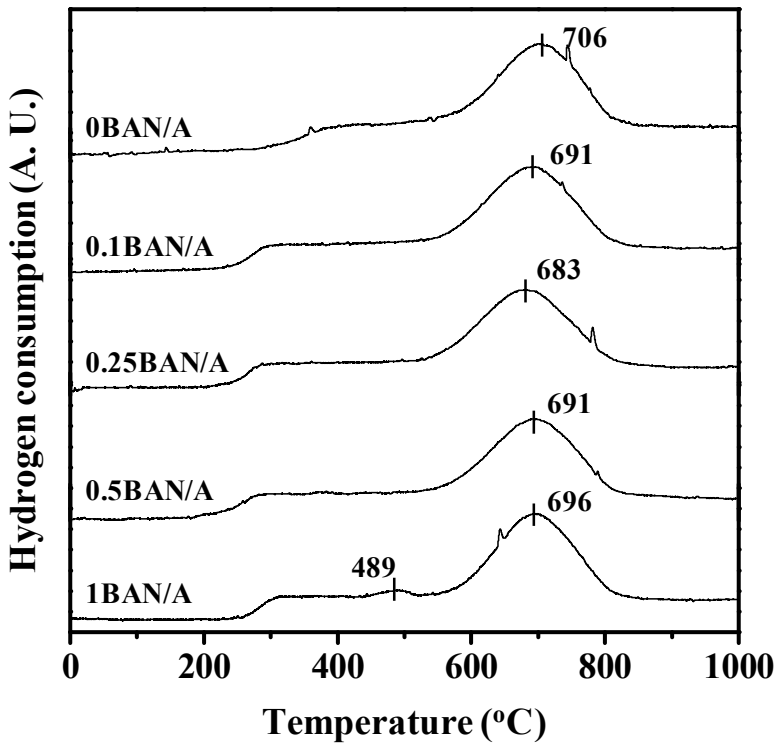

Fig. 3.27. TPR profiles of calcined xBAN/A catalysts.

3.4.6. Characterization of reduced catalysts

H_2-TPD experiments on reduced xBAN/A catalysts were performed and their corresponding profiles are shown in Fig. 3.28. Three different hydrogen desorption peaks appeared in all the xBAN/A catalysts. According to the literature [75], hydrogen desorption peak centered at around 200 ^{o}C is ascribed to weakly adsorbed hydrogen molecules on active metal sites, and hydrogen desorption peak centered at around 500 ^{o}C is due to strongly adsorbed hydrogen on metal sites. However, desorption peak above 600 ^{o}C is assigned to hydrogen spillover species. Therefore, total amount of hydrogen uptake on active nickel species can be obtained by integrating deconvoluted peaks below 600 ^{o}C. Deconvolution of the TPD profiles was performed using the OriginLab software. Nickel dispersion was calculated using the amount of hydrogen uptake as summarized in Table 3.10. It should be noted that the amount of total hydrogen uptake increased with increasing butyric acid/Ni ratio up to 0.25, and then the amount of hydrogen uptake decreased with increasing butyric acid/Ni ratio over 0.25. The nickel dispersion calculated from the amount of hydrogen uptake showed the same trend. According to the previous research [22], an appropriate amount of fatty acid surrounding nickel particles acts as a dispersing agent, inhibiting sintering of nickel particles during the thermal treatment. In the presence of excess fatty acid, however, nickel particles were fully surrounded by a fatty acid shell and uplifted from support, resulting in more opportunity to migrate and combine with other metal particles nearby. In a similar manner in this work, high dispersion of

nickel species could be achieved when medium amount of butyric acid was introduced.

CH_4-TPD experiments on reduced xBAN/A catalysts were performed and their corresponding profiles are shown in Fig. 3.29. Broad desorption peaks were observed for all the catalysts. For precise quantification, deconvolution of the CH_4-TPD profiles was conducted. According to the literature [76], the peak appearing below 700 ^oC is known to be related to the desorption of methane from the reduced nickel species. On the other hand, methane desorption peak at around 800 ^oC is related to the desorption of methane from alumina support [26]. Also, it is strong methane adsorption sites which can effectively stabilize adsorbed methane in the dissociative methane adsorption reaction, that is, rate-determining step. In this work, therefore, deconvoluted desorption peak area between 400 and 700 ^oC was only considered for quantification. The amount of desorbed methane was calculate by integrating the deconvoluted peak between 400 and 700 ^oC as summarized in Table 3.11. It was found that the amount of desorbed methane was greatly affected by butyric acid/Ni molar ratio. The amount of desorbed methane decreased in the order of 0.25BAN/A > 0.5BAN/A > 1BAN/A > 0.1BAN/A ≥ 0BAN/A. This trend was well consistent with the trend of nickel dispersion calculated by H_2-TPD measurements (Table 3.10). In other words, a xBAN/A catalyst with higher nickel dispersion showed higher methane adsorption capacity.

Qian et al. have reported that partially or fully dehydrogenated methane is desorbed from nickel/alumina catalyst below 700 ^oC [26]. It has also been reported that dehydrogenated methane species are major reaction

intermediates in the methane reforming [77,78]. From the above researches, it can be inferred that a nickel/alumina catalyst with high methane adsorption capacity will dissociate much amount of methane effectively in the reforming reaction. The dissociative adsorption of methane into dehydrogenated carbon species is known as the rate-determining step of reforming reactions [45-47]. Therefore, it is expected that the xBAN/A catalyst with higher methane adsorption capacity will show a better catalytic performance in the steam reforming of natural gas.

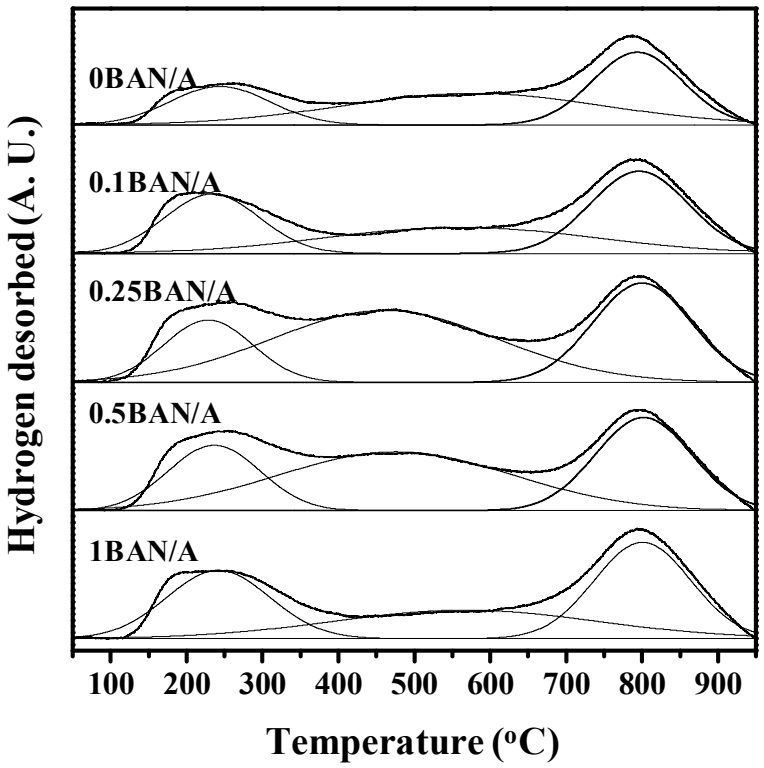

Fig. 3.28. H_2-TPD profiles of reduced xBAN/A catalysts.

Table 3.10

H_2-TPD results of reduced xBAN/A catalysts

Catalyst	Amount of desorbed hydrogen (μmol-H_2/g)[a]			Nickel dispersion[b] (%)
	Weak site (< 300 °C)	Strong site (300-600 °C)	Total	
0BAN/A	18	38	56	7.2
0.1BAN/A	26	33	59	7.6
0.25BAN/A	26	75	101	13.0
0.5BAN/A	28	64	92	11.9
1BAN/A	33	35	68	8.8

[a] Calculated from deconvoluted peak area of H_2-TPD profiles in Fig. 3.28
[b] Calculated by assuming $H/Ni_{atom} = 1$

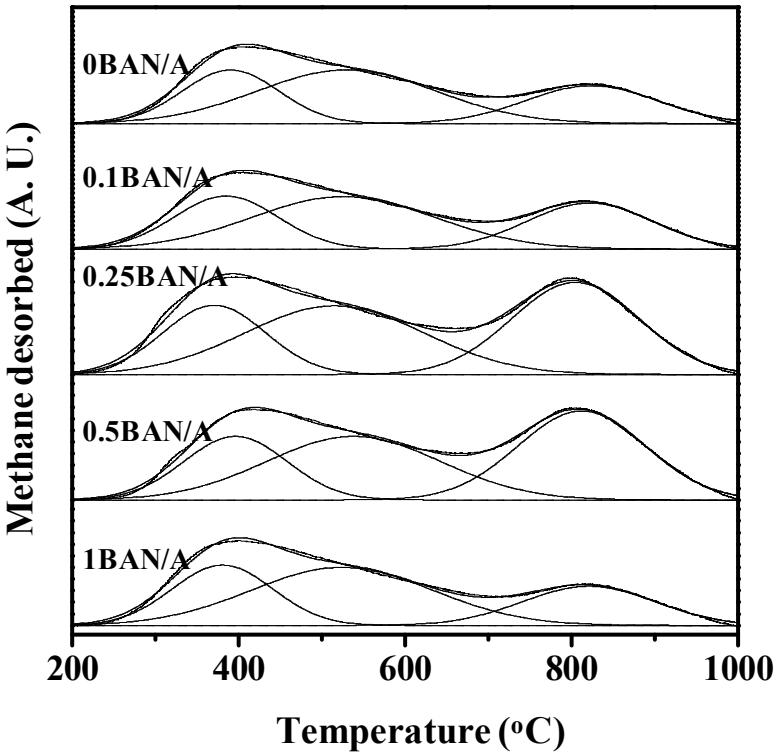

Fig. 3.29. CH_4-TPD profiles of reduced xBAN/A catalysts.

Table 3.11

CH_4-TPD results of reduced xBAN/A catalysts

Catalyst	Amount of desorbed methane (μmol-CH_4/g)[a]
0BAN/A	12.0
0.1BAN/A	12.0
0.25BAN/A	15.4
0.5BAN/A	13.8
1BAN/A	13.2

[a] Calculated from deconvoluted peak area of CH_4-TPD profiles in Fig. 3.29

3.4.7. Catalytic performance in the steam reforming of natural gas

Fig. 3.30 shows the catalytic activities of xBAN/A catalysts in the steam reforming of natural gas at 550 ^{o}C. The reaction was performed for 1000 min. It was observed that all the catalysts maintained initial catalytic activity with no significant deactivation. In commercial steam reforming process, nickel-based catalysts undergo activity drop caused by the growth of large nickel particles and the consequent reduction of active surface area [79]. Carbon formation on the catalyst surface is another problem which results in the loss of active sites by encapsulating the catalyst surface or blocking pores of the catalysts [80]. When considering the stable catalytic performance of xBAN/A catalysts, all the catalysts are believed to retain a strong resistance toward sintering and carbon deposition because of finely dispersed nickel particles on alumina support with well-developed mesopores.

Fig. 3.31 shows the catalytic activity of xBAN/A catalysts in the steam reforming of natural gas plotted as a function of butyric acid (BA)/Ni molar ratio. Volcano-shaped trends were observed with respect to butyric acid/Ni molar ratio. 0.25BAN/A catalyst treated with medium amount of butyric acid exhibited the best catalytic performance. This result was due to high methane adsorption capacity of 0.25BAN/A catalyst caused by high nickel dispersion. According to our previous studies [81,82], a nickel-based catalyst with high nickel dispersion retains a lot of active sites for steam reforming. Small nickel crystallite in finely dispersed nickel-based catalysts usually contains high proportion of step sites. The step sites are known to facilitate dehydrogenation

of methane and ethane, which is the rate-determining step of steam reforming reaction. Thus, it is evident that the xBAN/A catalyst with high nickel dispersion and high methane adsorption capacity showed high catalytic performance in the steam reforming of natural gas.

Fig. 3.32 shows the correlations between hydrogen yield and nickel dispersion, and between hydrogen yield and methane adsorption capacity of xBAN/A catalysts. A distinctive feature is that hydrogen yield increased with increasing nickel dispersion and with increasing methane adsorption capacity. On the basis of H_2-TPD and CH_4-TPD analyses, it is believed that an optimal butyric acid/Ni molar ratio was required for the highest nickel dispersion and methane adsorption capacity, and in turn, for the highest hydrogen yield in the steam reforming of natural gas.

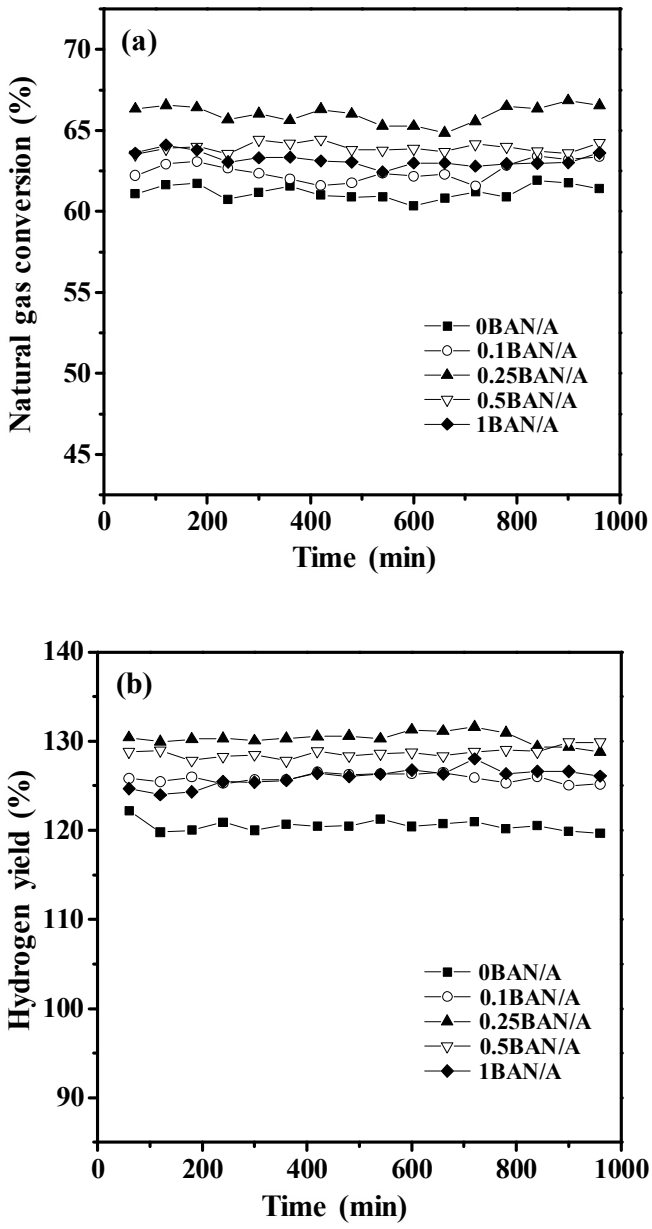

Fig. 3.30. Catalytic performances with time on stream: (a) Natural gas conversion and (b) hydrogen yield.

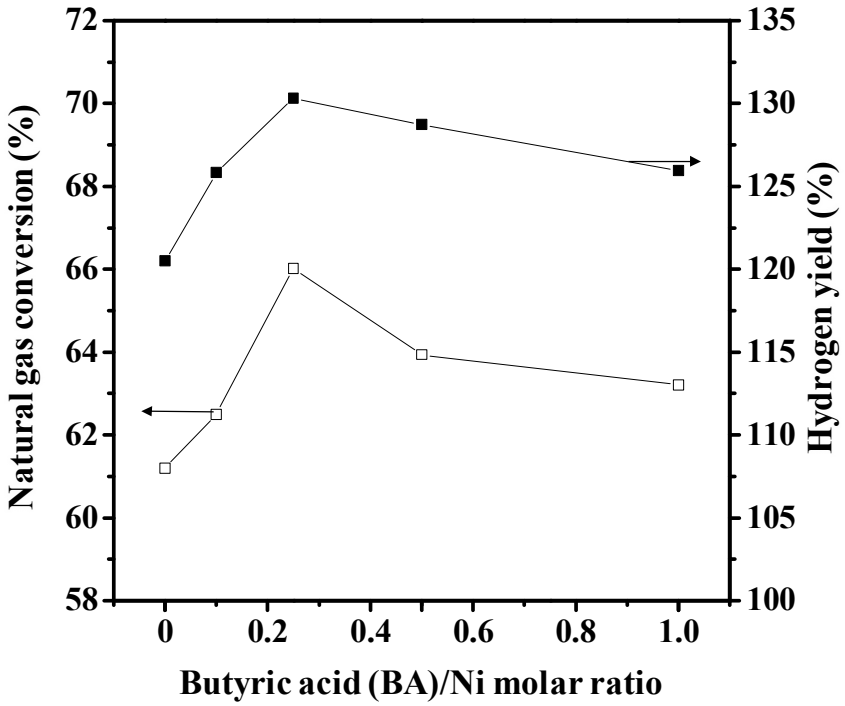

Fig. 3.31. Average catalytic performances during a 1000-min reaction over xBAN/A catalysts, plotted as a function of butyric acid (BA)/Ni molar ratio.

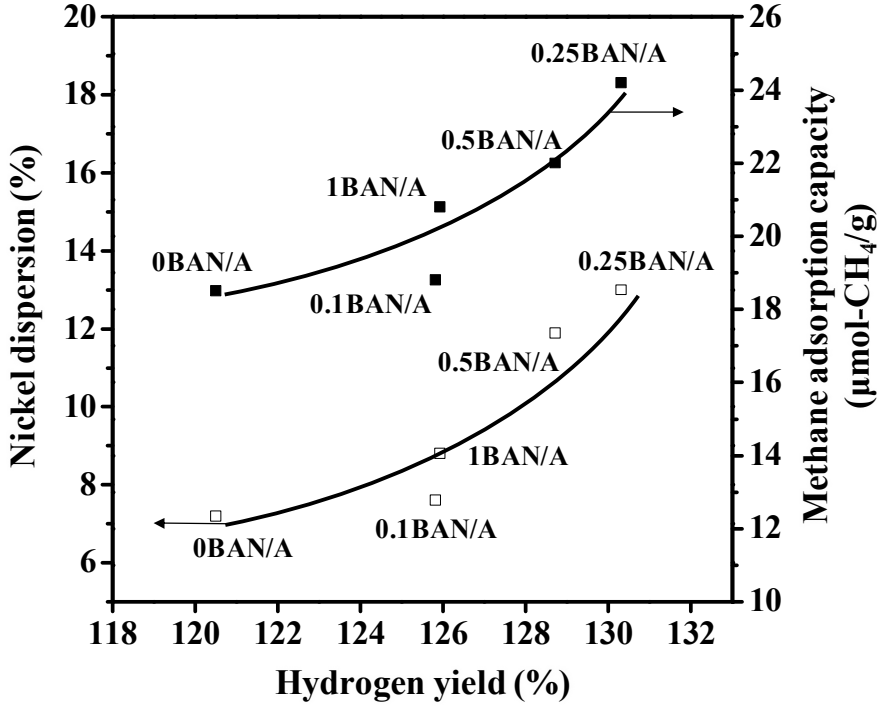

Fig. 3.32. Correlations between hydrogen yield and nickel dispersion, and between hydrogen yield and methane adsorption capacity of xBAN/A catalysts.

Chapter 4. Conclusions

Nickel/alumina catalysts were modified by various preparation methods including alkaline earth metal addition, supercritical CO_2 drying, vanadium addition, and butyric acid-assisted impregnation methods. They were applied to the hydrogen production by steam reforming of natural gas and were characterized by various techniques.

A series of mesoporous alkaline earth metal-promoted nickel-alumina xerogel (M/NA, M = Mg, Ca, Sr, and Ba) catalysts were prepared by a single-step epoxide-driven sol-gel method and a subsequent incipient wetness impregnation method. For comparison, mesoporous nickel-alumina xerogel catalyst (NA) without promoter was also prepared by a single-step epoxide-driven sol-gel method. Although all the reduced catalysts showed finely dispersed metallic nickel species, nickel dispersion of the reduced catalysts decreased in the order of Mg/NA > Sr/NA > Ca/NA > NA > Ba/NA. In the steam reforming of natural gas, natural gas conversion and hydrogen yield increased with increasing nickel surface area. The amount of carbon deposition decreased in all the alkaline earth metal-promoted catalysts with decreasing acidity of the catalysts. Among the catalysts tested, Mg/NA catalyst with the highest nickel surface area and the small amount of carbon deposition showed the best catalytic performance in hydrogen production by steam reforming of natural gas.

A magnesium-doped nickel-alumina aerogel catalyst (Mg/NAA) was prepared by an epoxide-driven sol-gel method, a supercritical CO_2 drying

method, and an incipient wetness impregnation method. For comparison, a magnesium-doped nickel-alumina xerogel catalyst (Mg/NAX) was also prepared without a supercritical CO_2 drying. Although both catalysts retained a well-defined mesoporous structure, Mg/NAA catalyst showed better textural properties than Mg/NAX catalyst. From XRD, TPR, TEM, and hydrogen chemisorption analyses, it was found that Mg/NAA catalyst retained higher nickel dispersion than Mg/NAX catalyst. In the steam reforming of natural gas, Mg/NAA catalyst with higher nickel dispersion showed higher natural gas conversion and hydrogen yield than Mg/NAX catalyst.

A series of vanadium-nickel-alumina (xVNA) catalysts were prepared by a single-step sol-gel method with a variation of vanadium loading (x, wt%) for use in the hydrogen production by steam reforming of natural gas. From XRD analyses of reduced xVNA catalysts, it was found that an appropriate amount of vanadium reduced nickel crystallite size. In the steam reforming of natural gas over xVNA catalysts, natural gas conversion and hydrogen yield showed volcano-shaped trends with respect to vanadium loading. It was revealed that natural gas conversion and hydrogen yield increased with decreasing nickel crystallite size.

A series of butyric acid (BA)-assisted nickel/alumina (xBAN/A, x = 0, 0.1, 0.25, 0.5, and 1) catalysts were characterized and evaluated in order to find an optimal butyric acid/Ni molar ratio (x) in the steam reforming of natural gas. Nickel dispersion of xBAN/A catalysts was improved when an appropriate amount of butyric acid was introduced due to the dispersing effect of butyric acid in thermal treatment step. xBAN/A catalysts with high nickel dispersion also showed high methane adsorption capacity. In the steam

reforming of natural gas, natural gas conversion and hydrogen yield increased with increasing nickel dispersion and with increasing methane adsorption capacity. Among the catalysts tested, 0.25BAN/A catalyst with the highest nickel dispersion and methane adsorption capacity showed the best catalytic performance.

In summary, physicochemical properties of nickel/alumina catalysts were modified by various preparation methods, including alkaline earth metal addition, supercritical CO_2 drying, vanadium addition, and butyric acid-assisted impregnation methods.. Various experimental measurements such as N_2 adsorption-desorption, XRD, TPR, TEM, SEM, FT-IR and chemisorption analyses were conducted to investigate the relationship between physicochemical properties and catalytic performances in the steam reforming of natural gas. Catalytic performance of the catalysts were greatly influenced by several physicochemical properties such as surface area, porosity, crystalline structure, reducibility, nickel dispersion, and methane adsorption capacity. Especially, it was found that nickel dispersion of reduced catalysts played an important role in determining overall catalytic activity in the hydrogen production by steam reforming of natural gas.

Bibliography

[1] I. Dincer, C. Acar. Int. J. Hydrogen Energy 42 (2017) 14843.

[2] M. Momirlana, T.N. Veziroglu. Int. J. Hydrogen Energy 30 (2005) 795.

[3] J. Goldemberg, Science 315 (2007) 808.

[4] S. Chu, A. Majumdar, Nature 488 (2012) 294.

[5] I. Dincer, Renew. Sustain. Energy Rev. 4 (2000) 157.

[6] H. Lund, Energy 32 (2007) 912.

[7] A. Haryanto, S. Fernando, N. Murali, S. Adhikari, Energy Fuels 19 (2005) 2098.

[8] A. Demirbas, Energ. Source. Part B 12(2) (2017) 172.

[9] C. Gillan, M. Fowles, S. French, S.D. Jackson, Ind. Eng. Chem. Res. 52 (2013) 13350.

[10] Y. Matsumura, T. Nakamori, Appl. Catal. A: Gen. 258 (2004) 258.

[11] N. Iwasa, T. Yamane, M. Arai, Int. J. Hydrogen Energy 36 (2011) 5904.

[12] A. Carrero, J.A. Calles, A.J. Vizcaino, Chem. Eng. J. 163 (2010) 395.

[13] K. Murata, L. Wang, M. Saito, M. Inaba, I. Takahara, et al., Energy Fuels 18 (2004) 122.

[14] Z.-X. Li, F.-B. Shi, L.-L. Li, T. Zhang, C.-H. Yan, Phys. Chem. Chem. Phys. 13 (2011) 2488.

[15] J.W. Han, C. Kim, J.S. Park, H. Lee, ChemSusChem 7 (2014) 451.

[16] L.Q. Nguyen, L.C. Abella, S.M. Gallardo, H. Hinode, React. Kinet. Catal. Lett. 93 (2008) 227.

[17] K. Kusakabe, K.-I. Sotowa, T. Eda, Y. Iwamoto, Fuel Process. Technol. 86 (2004) 319.

[18] H. Wu, V.L. Parola, G. Pantaleo, F. Puleo, A.M. Venezia, et al., Catalysts 3 (2013) 563.

[19] K.O. Christensen, D. Chen, R. Lødeng, A. Holmen, Appl. Catal. A: Gen

314 (2006) 9.

[20] J. Zhu, X. Peng, L. Yao, D. Tong, C. Hu, Catal. Sci. Technol. 2 (2012) 529.

[21] Y. Bang, S.J. Han, J. Yoo, J.H. Choi, K.H. Kang, et al. Int. J. Hydrogen Energy 38 (2013) 8751.

[22] S. Mo, E.T. Saw, Y. Du, A. Borgna, M.L. Ang, et al., Int. J. Hydrogen Energy 40 (2015) 13388.

[23] J.G. Seo, M.H. Youn, J.C. Jung, I.K. Song, Int. J. Hydrogen Energy 35 (2010) 6738.

[24] J.G. Seo, M.H. Youn, D.R. Park, J.C. Jung, I.K. Song, Catal. Lett. 132 (2009) 395.

[25] D.F. Tatterson, R.L. Mieville, Ind. Eng. Chem. Res. 27 (1988) 1595.

[26] K.S.W. Sing, D.H. Everett, R.A.W. Haul, L. Moscou, R.A. Pierotti, et al., Pure Appl. Chem. 57 (1985) 603.

[27] H. Choi, S.R. Al-Abed, S. Agarwal, D.D. Dionysiou, Chem. Mater. 20 (2008) 3649.

[28] Z. Luan, J.Y. Bae, L. Kevan, Chem. Mater. 12 (2000) 3202.

[29] P. Kim, Y. Kim, H. Kim, I.K. Song, J. Yi, J. Mol. Catal. A: Chem. 231 (2005) 247.

[30] J.A. Wang, A. Morales, X. Bokhimi, O. Novaro, T. Lopez, et al., Chem. Mater. 11 (1999) 308.

[31] X. Zhu, P. Huo, Y. Zhang, D. Cheng, C. Liu, Appl. Catal. B: Environ. 81 (2008) 132.

[32] J.G. Seo, M.H. Youn, S. Park, J. Lee, S.H. Lee, et al, Korean J. Chem. Eng. 25 (2008) 95.

[33] Y. Choi, N.D. Kim, J. Baek, W. Kim, H.J. Lee, et al., Int. J. Hydrogen Energy 36 (2011) 3844.

[34] P. Salagre, J.L.G. Fierro, F. Medina, J.E. Sueiras, J. Mol. Catal. A: Chem. 106 (1996) 125.

[35] J. Zielinski, Catal. Lett. 12 (1992) 389.

[36] Y. Bang, S.J. Han, J.G. Seo, M.H. Youn, J.H. Song, et al., Int. J. Hydrogen Energy 37 (2012) 17967.

[37] G. Li, L. Hu, J.M. Hill, Appl. Catal. A: Gen. 301 (2006) 16.

[38] J.D.S. Lisboa, D.C.R.M. Santos, F.B. Passos, F.B. Noronha, Catal. Today 101 (2005) 15.

[39] E. Ruckenstein, Y.H. Hu, Appl. Catal. A: Gen. 183 (1999) 85.

[40] K. Tomishige, Y. Chen, K. Fujimoto, J. Catal. 181 (1999) 91.

[41] Y.H. Hu, E. Ruckenstein, Catal. Lett. 36 (1996) 145.

[42] M.R. Gelsthorpe, K.B. Mok, J.R.H. Ross, J. Mol. Catal. 25 (1984) 253.

[43] S. Natesakhawat, O. Oktar, U.S. Ozkan, J. Mol. Catal. A: Chem. 241 (2005) 133.

[44] Y. Bang, J.G. Seo, M.H. Youn, I.K. Song, Int. J. Hydrogen Energy 37 (2012) 1436.

[45] J. Sehested, Catal. Today 111 (2006) 103.

[46] C.A. Bernardo, I. Alstrup, J.R. Rostrup-Nielsen, J. Catal. 96 (1985) 517.

[47] P. Munster, H.J. Grabke, J. Catal. 72 (1981) 279.

[48] T. Horiuchi, K. Sakuma, T. Fukui, Y. Kubo, T. Osaki, et al., Appl. Catal. A: Gen. 144 (1996) 111.

[49] M.S. Batista, R.K.S. Santos, E.M. Assaf, J.M. Assaf, E.A. Ticianelli, J. Power Sources 124 (2003) 99.

[50] K. Tanabe, Y. Fukuda, React. Kinet. Catal. Lett. 1 (1974) 21.

[51] Y.W. Chen, H.Y. Chen, W.F. Lin, React. Kinet. Catal. Lett. 65 (1998) 83.

[52] A. Papaioannou, H.W. Haynes, Jr., Energy Fuels 4 (1990) 38.

[53] T.F. Baumann, A.E. Gash, S.C. Chinn, A.M. Sawvel, R.S. Maxwell, et al., Chem. Mater. 17 (2005) 395.

[54] T. Błaszczyński, A. Ślosarczyk, M. Morawski, Procedia Eng. 57 (2013) 200.

[55] N. Hüsing, U. Schubert, Angew. Chem. Int. Ed. 37 (1998) 22.

[56] J.G. Seo, M.H. Youn, H.-I. Lee, J.J. Kim, E. Yang, et al., Chem. Eng. J. 141 (2008) 298.

[57] M.R. Awual, T. Yaita, Y. Miyazaki, D. Matsumura, H. Shiwaku, et al., Sci. Rep. 6 (2016) 19937.

[58] Y.-S. Jung, W.-L. Yoon, Y.-S. Seo, Y.-W. Rhee, Catal. Commun. 26 (2012) 103.

[59] A. Tribalis, G.D. Panagiotou, K. Bourikas, L. Sygellou, S. Kennou, et al., Catalysts 6 (2016) 11.

[60] V.V. Thyssen, T.A. Maia, E.M. Assaf, J. Braz. Chem. Soc. 26 (2015) 22.

[61] P. Kowalik, K. Antoniak-Jurak, M. Błesznowski, M.C. Herrera, M.A. Larrubia, et al., Catal. Today 254 (2015) 129.

[62] M.H. Youn, J.G. Seo, K.M. Cho, J.C. Jung, H. Kim, et al., Korean J. Chem. Eng. 25 (2008) 236.

[63] G. Du, S. Lim, Y. Yang, C. Wang, L. Pfefferle, et al., Appl. Catal. A Gen. 302 (2006) 48.

[64] J.G. Seo, M.H. Youn, J.S. Chung, I.K. Song, J. Ind. Eng. Chem. 16 (2010) 795.

[65] S. Mourdikoudis, L.M. Liz-Marzán, Chem. Mater. 25 (2013) 1465.

[66] Z.-F Pei, V. Ponec, Appl. Surf. Sci. 103 (1996) 171.

[67] S. Wu, L. Fu, M. Su, M. Aslam, K.C. Wong, et al., Nano Lett. 4(2) (2004) 383.

[68] S.M. Morris, P.F. Fulvio, M. Jaroniec, J. Am. Chem. Soc. 130 (2008) 15210.

[69] H.M. Gobara, M.M. Gomaa, Pet. Sci. Technol. 27 (2009) 1572.

[70] M.K. Nazemi, S. Sheibani, F. Rashchi, V.M. Gonzalez-DelaCruz, A. Caballero, Adv. Powder Technol. 23 (2012) 833.

[71] E.D. Dimotakis, T.J. Pinnavaia, Inorg. Chem. 29 (1990) 2393.

[72] M. Zangouei, A.Z. Moghaddam, M. Arasteg, Chem. Eng. Res. Bull. 14 (2010) 97.

[73] L. Zhang, Y. Zhang, RSC Adv. 5 (2015) 62173.

[74] M.A. Goula, N.D. Charisiou, K.N. Papageridis, A. Delimitis, E. Pachatouridou, et al., Int. J. Hydrogen Energy 40(30) (2015) 9183.

[75] S. Velu, S.K. Gangwal, Solid State Ionics 177 (2006) 803.

[76] S. Park, J. Yoo, S.J. Han, J.H. Song, E.J. Lee, et al., Int. J. Hydrogen Energy 42 (2017) 15096.

[77] K. Hou, R. Hughes, Chem. Eng. J. 82 (2001) 311.

[78] C. Wang, S. Sun, W. Wei, Y. Zhao, Int. J. Hydrogen Energy 41(42) (2016) 19014.

[79] J. Sehested, J.A.P. Gelten, I.N. Remediakis, H. Bengaard, J.K. Nørskov, J. Catal. 223 (2004) 432.

[80] M.C. Annesini, V. Piemonte, L. Turchetti, Chem. Eng. Trans. 11 (2007) 21.

[81] J.G. Seo, M.H. Youn, Y. Bang, I.K. Song, Int. J. Hydrogen Energy 36 (2011) 3505.

[82] Y. Bang, S. Park, S.J. Han, J. Yoo, J.H. Song, et al., Appl. Catal. B: Environ 180 (2016) 179.

초 록

화석 연료의 고갈과 지구 온난화에 대한 우려가 커짐에 따라 지속 가능한 신재생 에너지에 대한 연구가 활발히 진행되고 있다. 여러 신재생 에너지 중에서도 수소는 에너지 밀도가 크고 환경 친화적이며 매장량이 풍부하기 때문에 가장 우수한 에너지 전달 매체 중의 하나로 각광을 받고 있다. 수소를 생산하는 방법으로는 에너지 전환율이 높고 경제성이 큰 천연가스의 수증기 개질 반응이 이용되고 있다. 천연가스의 수증기 개질 반응에는 니켈계 촉매가 높은 반응 활성을 나타낸다고 알려져 있다. 그러나 니켈계 촉매는 니켈 소결 및 탄소 침적에 의한 비활성화에 취약하다는 단점이 있다. 따라서 높은 반응 활성과 우수한 안정성을 갖는 신규 촉매를 개발하는 것이 매우 중요하다고 할 수 있다.

본 연구에서는 천연가스의 수증기 개질 반응에서 니켈/알루미나 촉매의 효율 향상을 위해 알칼리 토금속 첨가, 초임계 이산화탄소 건조법, 바나듐 첨가, 부티르 산을 이용한 함침법 등을 이용하였다.

우선, 단일공정 에폭사이드 유도 졸-겔법 및 초기습윤함침법으로 알칼리 토금속이 첨가된 중형기공성 니켈-알루미나 제로젤 (M/NA, M = Mg, Ca, Sr 및 Ba) 촉매를 제조하였다. 비교를 위해 알칼리 토금속이 첨가되지 않은 중형기공성 니켈-알루미나 제로젤 (NA) 촉매를 단일공정 에폭사이드 유도 졸-겔법으로 제조하였다. 수소 흡착 분석 결과 니켈 표면적은 Mg/NA > Sr/NA > Ca/NA > NA > Ba/NA의 순서로 감소하는 것을 확인할 수 있었다. NA 촉매와 M/NA 촉매를

천연가스의 수증기 개질 반응에 적용시킨 결과, 촉매 활성과 니켈 표면적이 양의 상관관계를 나타내는 것을 확인할 수 있었다. 제조된 촉매 중에서 니켈 표면적이 가장 넓은 Mg/NA가 가장 높은 반응 활성을 나타내었다. 반응 후 촉매의 탄소량 분석 결과 M/NA 촉매가 NA 촉매에 비해 탄소 침적이 적게 일어난 것을 확인하였다.

상기 촉매 중 가장 우수한 성능을 나타낸 Mg/NA 촉매를 더 개선하기 위해 단일공정 에폭사이드 유도 졸-겔법 및 초임계 이산화탄소 건조법과 초기습윤함침법을 이용하여 마그네슘이 첨가된 중형기공성 니켈-알루미나 에어로젤 (Mg/NAA) 촉매를 제조하였다. 비교를 위해 상기 Mg/NA 촉매와 유사한 방법으로 마그네슘이 첨가된 중형기공성 니켈-알루미나 제로젤 (Mg/NAX) 촉매를 제조하였다. 초임계 이산화탄소 건조법을 이용하여 제조된 Mg/NAA 촉매가 Mg/NAX 촉매에 비해 넓은 비표면적, 큰 기공 부피 및 기공 크기를 나타내었다. 이는 에어로젤의 건조 과정에서 니켈-알루미나 겔의 네트워크 구조가 붕괴되는 현상이 억제되었기 때문이라고 판단된다. 비표면적이 넓은 Mg/NAA 촉매는 Mg/NAX 촉매에 비해 넓은 니켈 표면적 및 높은 니켈 분산도를 나타내었다. 메탄 승온 탈착 분석 결과 Mg/NAA 촉매가 Mg/NAX 촉매에 비해 우수한 메탄 친화도를 보이는 것을 확인하였다. Mg/NAA 촉매와 Mg/NAX 촉매를 천연가스의 수증기 개질 반응에 적용시킨 결과 높은 니켈 분산도 및 메탄 친화도를 갖는 Mg/NAA 촉매가 더 높은 천연가스 전환율과 수소 수율을 나타내는 것을 확인할 수 있었다.

다양한 바나듐 담지량을 갖는 중형기공성 바나듐-니켈-알루미나 제조젤 (xVNA, x = 0, 0.5, 1.0, 1.5 및 2.0) 촉매를 단일공정 에폭사이드 유도 졸-겔법을 이용하여 제조하였다. TPR

분석 결과 바나듐이 첨가된 촉매에서 니켈 환원성이 향상된 것을 확인하였다. 환원된 촉매의 XRD 분석을 통해 적절한 양의 바나듐이 첨가되었을 경우 니켈 결정 크기가 작아지는 것을 확인할 수 있었다. xVNA 촉매를 천연가스의 수증기 개질 반응에 적용시킨 결과 천연가스 전환율과 수소 수율이 바나듐 담지량에 따라 화산형의 개형을 나타내었다. 제조된 촉매 중에서 1.0 wt%의 바나듐이 담지된 촉매가 가장 작은 니켈 결정 크기 및 가장 우수한 반응활성을 나타내었다.

함침 과정에서 다양한 부티르 산/니켈 몰 비(x)를 적용한 중형기공성 니켈/알루미나 제로젤 (xBAN/A) 촉매를 제조하였다. 함침 과정에서 적절한 양의 부티르 산이 첨가되었을 경우 니켈 입자를 둘러싼 부티르 산의 입체장애로 인해 니켈 분산도가 향상되는 것을 확인할 수 있었다. 적절한 양의 부티르 산이 첨가될 경우 촉매 반응 활성과 직접적인 관련성이 있는 메탄 흡착 능력 또한 향상되는 것을 확인하였다. 제조된 촉매를 천연가스의 수증기 개질 반응에 적용시킨 결과 반응 활성이 부티르 산/니켈 몰 비에 따라 화산형의 개형을 나타내었다. 제조된 촉매 중에서 0.25BAN/A 촉매가 가장 높은 니켈 분산도 및 반응활성을 나타내었다.

요약하면, 본 연구에서는 다양한 니켈/알루미나 촉매를 제조하여 천연가스의 수증기 개질 반응에 적용시켰다. 촉매의 물리화학적 특성이 천연가스의 수증기 개질 반응 활성에 미치는 영향을 설명하기 위해 질소 흡탈착, XRD, TPR, TEM, SEM, H_2-TPD, CH_4-TPD 및 FT-IR 등의 다양한 분석을 수행하였다. 결과적으로, 니켈의 분산도가 천연가스의 수증기 개질 반응을 통한 수소 생산에서 촉매 활성을 결정짓는 중요한 인자임을 확인하였다.

주요어: 수소 생산, 천연가스의 수증기 개질, 니켈 촉매, 알칼리토금속, 초임계 이산화탄소 건조법, 바나듐, 부티르 산

학 번: 2015-30216

List of publications

Papers

International papers published (First author)

1. **J. Yoo**, S. Park, J.H. Song, S. Yoo, I.K. Song, "Hydrogen Production by Steam Reforming of Natural Gas over Vanadium-nickel-alumina Catalysts", *Journal of Nanoscience and Nanotechnology* (In press).

2. **J. Yoo**, S. Park, J.H. Song, S. Yoo, I.K. Song, "Hydrogen Production by Steam Reforming of Natural Gas over Butyric Acid-assisted Nickel/alumina Catalyst", *International Journal of Hydrogen Energy*, 42, pp.28377-28385 (2017).

3. **J. Yoo**, Y. Bang, S.J. Han, S. Park, J.H. Song, I.K. Song, "Hydrogen Production by Steam Reforming of Liquefied Natural Gas (LNG) over Magnesium-doped Nickel-alumina Aerogel Catalyst", *Journal of Nanoscience and Nanotechnology*, 16(10), pp.10835-10840 (2016).

4. **J. Yoo**, Y. Bang, S.J. Han, S. Park, J.H. Song, I.K. Song, "Hydrogen Production by Tri-reforming of Methane over Nickel-alumina Aerogel Catalyst", *Journal of Molecular Catalysis A: Chemical*, 410, pp.74-80 (2015).

5. **J. Yoo**, Y. Bang, S.J. Han, T.H. Kang, J. Lee, I.K. Song, "Hydrogen Production by Steam Reforming of Liquefied Natural Gas (LNG) over Mesoporous Alkaline Earth Metal-promoted Nickel-alumina Xerogel Catalysts", *Journal of Molecular Catalysis A: Chemical*, 380, pp.28-33 (2013).

International papers published (Co-author)

1. S. Park, **J. Yoo**, S.J. Han, J.H. Song, E.J. Lee, I.K. Song, "Steam Reforming of Liquefied Natural Gas (LNG) for Hydrogen Production over Nickel-boron-alumina Xerogel Catalyst", *International Journal of Hydrogen Energy*, 42(22), pp.15096-15106 (2017).

2. J.H. Song, S. Yoo, **J. Yoo**, S. Park, M.Y. Gim, T.H. Kim, I.K. Song, "Hydrogen Production by Steam Reforming of Ethanol over Ni/Al_2O_3-La_2O_3 Xerogel Catalysts", *Molecular Catalysis*, 434, pp.123-133 (2017).

3. S. Park, S.J. Han, **J. Yoo**, J.H. Song, E.J. Lee, I.K. Song, "Hydrogen Production by Steam Reforming of Liquefied Natural Gas (LNG) over Nickel-iron-alumina Aerogel Catalyst", *Journal of Nanoscience and Nanotechnology*, 17(11), pp.8248-8254 (2017).

4. S.J. Han, J.H. Song, **J. Yoo**, S. Park, K.H. Kang, I.K. Song, "Sorption-enhanced Hydrogen Production by Steam Reforming of Ethanol over Mesoporous $Co/CaO-Al_2O_3$ Xerogel Catalysts: Effect of Ca/Al Molar Ratio", *International Journal of Hydrogen Energy*, 42(9), pp.5886-5898 (2017).

5. J.H. Song, S.J. Han, **J. Yoo**, S. Park, D.H. Kim, I.K. Song, "Hydrogen Production by Steam Reforming of Ethanol over $Ni-Sr-Al_2O_3-ZrO_2$ Aerogel Catalyst", *Journal of Molecular Catalysis A: Chemical*, 424, pp.342-350 (2016).

6. J.H. Song, S.J. Han, **J. Yoo**, S. Park, D.H. Kim, I.K. Song, "Effect of Sr Content on Hydrogen Production by Steam Reforming of Ethanol over $Ni-Sr/Al_2O_3-ZrO_2$ Xerogel Catalysts", *Journal of Molecular Catalysis A: Chemical*, 418-419, pp.68-77 (2016).

7. Y. Bang, S. Park, S.J. Han, **J. Yoo**, J.H. Choi, T.H. Kang, J. Lee, I.K, Song, "Hydrogen Production by Steam Reforming of Liquefied Natural Gas (LNG) over Nickel-phosphorus-alumina Xerogel Catalyst Prepared by a Carbon-templating Epoxide-driven Sol-gel Method", *Journal of Nanoscience and Nanotechnology*, 16, pp.4605-4611 (2016).

8. J.H. Song, J.O. Jun, K.H. Kang, S.J. Han, **J. Yoo**, S. Park, D.H. Kim, I.K. Song, "Synthesis of Dimethyl Carbonate from Propylene Carbonate and Methanol over Y_2O_3/CeO_2-La_2O_3 Catalysts", *Journal of Nanoscience and Nanotechnology*, 16(10), pp.10810-10815 (2016).

9. J.H. Song, S.J. Han, **J. Yoo**, S. Park, D.H. Kim, I.K. Song, "Hydrogen Production by Steam Reforming of Ethanol over Ni-X/Al_2O_3-ZrO_2 (X=Mg, Ca, Sr, and Ba) Xerogel Catalysts: Effect of Alkaline Earth Metal Addition", *Journal of Molecular Catalysis A: Chemical*, 415, pp.151-159 (2016).

10. S.J. Han, J.H. Song, Y. Bang, **J. Yoo**, S. Park, K.H. Kang, I.K. Song, "Hydrogen Production by Steam Reforming of Ethanol over Mesoporous Cu-Ni-Al_2O_3-ZrO_2 Xerogel Catalysts", *International Journal of Hydrogen Energy*, 41(4), pp.2554-2563 (2016).

11. S.J. Han, Y. Bang, J.H. Song, **J. Yoo**, S. Park, K.H. Kang, I.K. Song, "Hydrogen Production by Steam Reforming of Ethanol over Dual-templated Ni-Al_2O_3 Catalyst", *Catalysis Today*, 265, pp.103-110 (2016).

12. Y. Bang, S. Park, S.J. Han, **J. Yoo**, J.H. Song, J.H. Choi, K.H. Kang, I.K. Song, "Hydrogen Production by Steam Reforming of Liquefied Natural Gas (LNG) over Mesoporous Ni/Al_2O_3 Catalyst Prepared by an EDTA-assisted Impregnation Method", *Applied Catalysis B: Environmental*, 180, pp.179-188 (2016).

13. S. Park, Y. Bang, S.J. Han, **J. Yoo**, J.H. Song, J.C. Song, J. Lee, I.K. Song, "Hydrogen Production by Steam Reforming of Liquefied Natural Gas (LNG) over Mesoporous Nickel-iron-alumina Catalyst", *International Journal of Hydrogen Energy*, 40(17), pp.5869-5877 (2015).

14. T.H. Kang, J.H. Choi, Y. Bang, **J. Yoo**, J.H. Song, W. Joe, J.S. Choi, I.K. Song, "Dehydration of Glycerin to Acrolein over $H_3PW_{12}O_{40}$ Heteropolyacid Catalyst Supported on Silica-alumina", *Journal of Molecular Catalysis A: Chemical*, 396, pp.282-289 (2015).

15. S.J. Han, Y. Bang, **J. Yoo**, S. Park, K.H. Kang, J.H. Choi, J.H. Song, I.K. Song, "Hydrogen Production by Steam Reforming of Ethanol over P123-assisted Mesoporous Ni-Al_2O_3-ZrO_2 Xerogel Catalysts", *International Journal of Hydrogen Energy*, 39(20), pp.10445-10453 (2014).

16. Y. Bang, S.J. Han, **J. Yoo**, S. Park, J.H. Choi, Y.J. Lee, J.H. Song, I.K. Song, "Hydrogen Production by Steam Reforming of Liquefied Natural Gas (LNG) over Mesoporous Nickel-phosphorus-alumina Aerogel Catalyst", *International Journal of Hydrogen Energy*, 39(10), pp.4909-4916 (2014).

17. J.H. Choi, T.H. Kang, Y. Bang, **J. Yoo**, J.O. Jun, I.K. Song, "Scanning Tunneling Microscopy Investigation of Nano-Structured α-$K_5PW_{11}(M{\cdot}OH_2)O_{39}$(M = Mn^{II}, Co^{II}, Ni^{II}, and Zn^{II}) Keggin Heteropolyacid Catalyst Monolayers", *Journal of Nanoscience and Nanotechnology*, 14(11), pp.8873-8878 (2014).

18. Y. Bang, S.J. Han, **J. Yoo**, J.H. Choi, J.K. Lee, J.H. Song, J. Lee, I.K. Song, "Hydrogen Production by Steam Reforming of Simulated Liquefied Natural Gas (LNG) over Nickel Catalyst Supported on Mesoporous Phosphorus-

modified Alumina Xerogel", *Applied Catalysis B: Environmental*, 148-149, pp.269-280 (2014).

19. S.J. Han, Y. Bang, **J. Yoo**, K.H. Kang, J.H. Song, J.G. Seo, I.K. Song, "Hydrogen Production by Steam Reforming of Ethanol over Mesoporous Ni-Al_2O_3-ZrO_2 Aerogel Catalysts", *International Journal of Hydrogen Energy*, 38(35), pp.15119-15127 (2013).

20. Y. Bang, S.J. Han, **J. Yoo**, J.H. Choi, K.H. Kang, J.H. Song, J.G. Seo, J.C. Jung, I.K. Song, "Hydrogen Production by Steam Reforming of Liquefied Natural Gas (LNG) over Trimethylbenzene-assisted Ordered Mesoporous Nickel-alumina Catalyst", *International Journal of Hydrogen Energy*, 38(21), pp.8751-8758 (2013).

21. S.J. Han, Y. Bang, **J. Yoo**, J.G. Seo, I.K. Song, "Hydrogen Production by Steam Reforming of Ethanol over Mesoporous Ni-Al_2O_3-ZrO_2 Xerogel Catalysts: Effect of Nickel Content", *International Journal of Hydrogen Energy*, 38(20), pp.8285-8292 (2013).

22. S.J. Han, Y. Bang, J.G. Seo, **J. Yoo**, I.K. Song, "Hydrogen Production by Steam Reforming of Ethanol over Mesoporous Ni-Al_2O_3-ZrO_2 Xerogel Catalysts: Effect of Zr/Al Molar Ratio", *International Journal of Hydrogen Energy*, 38(3), pp.1376-1383 (2013).

Patents

Registered patents

1. 송인규, 한승주, **유재경**, 박승원, 송지환, 이현주, “단일공정 졸-겔(Sol-gel)법으로 제조된 중형기공성 니켈-구리-알루미나-지르코니아 제로젤 촉매, 그 제조 방법 및 상기 촉매를 이용한 에탄올의 수증기 개질 반응에 의한 수소가스 제조 방법”, 대한민국특허 제 1,795,477호 (2017).

2. 송인규, 한승주, 방용주, **유재경**, 박승원. 이현주, “이온성 액체를 이용한 중형기공성 니켈-알루미나 촉매의 제조, 그 촉매 및 상기 촉매를 이용한 수소가스 제조 방법”, 대한민국특허 제 1,659,264호 (2016).

3. 송인규, 방용주, 박승원, 한승주, **유재경**, 이현주, “알루미나 담체에 화학적으로 고정화된 니켈 촉매, 그 제조 방법 및 상기 촉매를 이용한 액화천연가스의 수증기 개질 반응에 의한 수소 가스 제조 방법”, 대한민국특허 제 1,636,005호 (2016).

4. 송인규, 박승원, 방용주, 한승주, **유재경**, 이현주, “중형기공성 니켈-철-알루미나 제로젤 촉매, 그 제조 방법 및 상기 촉매를 이용한 액화천연가스의 수증기 개질 반응에 의한 수소 가스 제조 방법”, 대한민국특허 제 1,628,695호 (2016).

5. 송인규, 방용주, 한승주, **유재경**, 이현주, “인을 포함한 중형기공성 알루미나 제어로젤 담체에 담지된 니켈 촉매, 그 제조 방법 및 상기 촉매를 이용한 액화천연가스의 수증기 개질 반응에 의한 수소가스 제조 방법”, 대한민국특허 제 1,512,505호 (2015).

6. 송인규, 방용주, 한승주, **유재경**, 이현주, “중형기공성 니켈-인-알루미나 에어로젤 촉매, 그 제조 방법 및 상기 촉매를 이용한 액화천연가스의 수증기 개질 반응에 의한 수소 가스 제조 방법”, 대한민국특허 제 1,460,348호 (2014).

Applied patents

1. 송인규, 송지환, 유상범, **유재경**, 박승원, “중형기공성 알루미나-란타나 복합 산화물 제로젤 담체에 담지된 니켈-코발트 이종금속 촉매, 그 제조 방법 및 상기 촉매를 이용한 에타올 수증기 개질 반응에 의한 수소 가스 제조 방법”, 대한민국 특허출원 10-2017-0119386 (2017).

2. 송인규, 한승주, **유재경**, 박승원, 송지환, “중형기공성 칼슘옥사이드-알루미나 제로젤 담체에 담지된 코발트 촉매, 그 제조 방법 및 상기 촉매를 이용한 에탄올의 수증기 개질 반응에 의한 수소가스 제조 방법”, 대한민국 특허출원 10-2016-0095933 (2016).

3. 송인규, 박승원, 한승주, **유재경**, 송지환, “중형기공성 니켈-붕소-알루미나 제로젤 촉매, 그 제조 방법 및 상기 촉매를 이용한 액화천연가스의 수증기 개질 반응에 의한 수소 가스 제조 방법”, 대한민국 특허출원 10-2016-0061001 (2016).

Conferences

International conferences (First author)

1. **J. Yoo**, S. Park, J.H. Song, I.K. Song, "Hydrogen Production by Steam Reforming of Natural Gas over Vanadium-nickel-alumina Catalysts", *NANO KOREA 2017*, P1705_0010, Kintex, Korea (2017/7/12-14).

2. **J. Yoo**, Y. Bang, S.J. Han, T.H. Kang, I.K. Song, "Alkaline Earth Metal-promoted Nickel-alumina Xerogel Catalysts for Hydrogen Production by Steam Reforming of Natural Gas", *APCChE 2015 Congress*, P-3126273, Melbourne, Australia (2015/9/27-2015/10/01).

3. **J. Yoo**, Y. Bang, S.J. Han, S. Park, J.H. Song, I.K. Song, "Hydrogen Production by Steam Reforming of Liquefied Natural Gas (LNG) over Magnesium-doped Nickel-alumina Aerogel Catalyst", *NANO KOREA 2015*, P1503_105, COEX, Seoul, Korea (2015/7/1-3).

4. **J. Yoo**, Y. Bang, S.J. Han, S. Park, J.H. Song, I.K. Song, "Methane Tri-reforming over Nickel-alumina Aerogel Catalyst", *The 15th Korea-Japan Symposium on Catalysis*, GP43, Busan, Korea (2015/5/26-28).

5. **J. Yoo**, Y. Bang, S.J. Han, T.H. Kang, I.K. Song, "Hydrogen Production by Steam Reforming of Liquefied Natural Gas (LNG) over Mesoporous Alkaline Earth Metal-promoted Nickel-alumina Xerogel Catalysts", *20th WHEC (World Hydrogen Energy Conference) 2014*, 52, Kwangju, Korea (2014/6/15-20).

6. **J. Yoo**, Y. Bang, S.J. Han, T.H. Kang, I.K. Song, "Effect of Promoter on Nickel-alumina Xerogel Catalyst for Hydrogen Production by Steam Reforming of Liquefied Natural Gas (LNG)", *International Conference on Hydrogen Production - 2014*, P-43, Fukuoka, Japan (2014/2/2-5).

International conferences (Co-author)

1. J.H. Song, M.Y. Gim, S.J. Han, **J. Yoo**, S. Park, I.K. Song, "Ni-Sr/Al_2O_3-ZrO_2 Catalysts for Hydrogen Production by Steam Reforming of Ethanol", *EUROPACT 2017*, IOD 1291, Florence, Italy (2017/8/27-31).

2. S. Park, T.H. Kim, E.J. Lee, S.J. Han, **J. Yoo**, J.H. Song, I.K. Song, "Mesoporous Nickel-iron-alumina Catalysts for Hydrogen Production by Steam Reforming of Liquefied Natural Gas (LNG)", *The 16th International Congress on Catalysis*, PC066, Beijing, China (2016/7/3-8).

3. S. Park, S.J. Han, **J. Yoo**, J.H, Song, E.J. Lee, I.K. Song, "Hydrogen Production by Steam Reforming of Liquefied Natural Gas (LNG) over Nickel-iron-alumina Aerogel Catalyst", *NANO KOREA 2016*, P1605_0546, KINTEX, Korea (2016/7/13-15).

4. T.H. Kang, J.H. Choi, Y. Bang, **J. Yoo**, J.H. Song, W. Joe, J.S. Choi, I.K. Song, "Dehydration of Glycerin to Acrolein over Tungstophosphoricacid ($H_3PW_{12}O_{40}$) Catalyst Supported on Silica-alumina", *APCChE 2015 Congress*, P-3126311, Melbourne, Australia (2015/9/27-2015/10/01).

5. S.J. Han, Y. Bang, J.H. Song, **J. Yoo**, S. Park, K.H. Kang, I.K. Song, "Hydrogen Production by Steam Reforming of Ethanol over Dual-templated Ni-Al_2O_3 Catalyst", *NANO KOREA 2015*, P1503_097, COEX, Seoul, Korea (2015/7/1-3).

6. J.H. Song, J.O. Jun, K.H. Kang, S.J. Han, **J. Yoo**, S. Park, D.H. Kim, I.K. Song, "Synthesis of Dimethyl Carbonate from Propylene Carbonate and Methanol over Y_2O_3/CeO_2-La_2O_3 Catalysts", *NANO KOREA 2015*, P1503_098, COEX, Seoul, Korea (2015/7/1-3).

7. Y. Bang, S.J. Han, **J. Yoo**, S. Park, J.H. Choi, J. Lee, I.K. Song, "Hydrogen Production by Steam Reforming of LNG over Nickel-phosphorus-alumina

Catalyst Prepared by a Templating Sol-gel Method", *NANO KOREA 2014*, P1406_001, COEX, Seoul, Korea (2014/7/2-4).

8. Y. Bang, S.J. Han, **J. Yoo**, J.H. Choi, J.K. Lee, I.K. Song, "Hydrogen Production by Steam Reforming of Liquefied Natural Gas (LNG) over Nickel Catalyst Supported on Mesoporous Phosphorus-modified Alumina Xerogel", *20th WHEC (World Hydrogen Energy Conference) 2014*, 58, Kwangju, Korea (2014/6/15-20).

9. S.J. Han, Y. Bang, **J. Yoo**, I.K. Song, "Hydrogen Production by Steam Reforming of Ethanol over Mesoporous Ni-Al_2O_3-ZrO_2 Aerogel Catalyst", *20th WHEC (World Hydrogen Energy Conference) 2014*, 56, Kwangju, Korea (2014/6/15-20).

10. S.J. Han, Y. Bang, **J. Yoo**, K.H. Kang, J.H. Song, J.G. Seo, I.K. Song, "Ethanol Steam Reforming over a Mesoporous Ni-Al_2O_3-ZrO_2 Aerogel Catalyst", *Seventh Tokyo Conference on Advanced Catalytic Science and Technology*, GP2035, Kyoto, Japan (2014/6/1-6).

11. Y. Bang, S.J. Han, **J. Yoo**, J.H. Choi, K.H. Kang, I.K. Song, "Preparation of Structure-modified Ordered Mesoporous Nickel-alumina Catalyst for Hydrogen Production by Steam Reforming of Liquefied Natural Gas (LNG)", *International Conference on Hydrogen Production - 2014*, P-45, Fukuoka, Japan (2014/2/2-5).

12. S.J. Han, Y. Bang, **J. Yoo**, I.K. Song, "Ethanol Steam Reforming over a Mesoporous Ni-Al_2O_3-ZrO_2 Xerogel Catalysts", *International Conference on Hydrogen Production - 2014*, P-44, Fukuoka, Japan (2014/2/2-5).

13. J.H. Choi, T.H. Kang, Y. Bang, **J. Yoo**, J.O. Jun, I.K. Song, "STM Investigation of Nano-structured α-$K_5PW_{11}O_{39}(M{\cdot}OH_2)$ ($M = Mn^{II}$, Co^{II}, Ni^{II}, and Zn^{II}) Heteropolyacid Catalyst Monolayers", *NANO Korea 2013 Symposium*, P1303_006, Coex, Seoul, Korea (2013/7/10-12).

14. S.J. Han, Y. Bang, J.G. Seo, **J. Yoo**, I.K. Song, "Hydrogen Production by Steam Reforming of Ethanol over Mesoporous Ni-Al_2O_3-ZrO_2 Xerogel Catalysts: Effect of Zr/Al Molar Ratio", *The 4th International Conference on New & Renewable Energy 2013*, P2-11, Daegu. Korea (2013/3/28-30).

15. Y. Bang, S.J. Han, J.G. Seo, **J. Yoo**, I.K. Song, "Hydrogen Production by Steam Reforming of Liquefied Natural Gas (LNG) over Ordered Mesoporous Nickel-alumina Catalyst", *The 4th International Conference on New & Renewable Energy 2013*, P2-9, Daegu. Korea (2013/3/28-30).

Domestic conferences (First author)

1. **유재경**, 박승원, 송지환, 유상범, 송인규, "계면활성제의 도입이 천연가스의 수증기 개질 반응용 니켈/알루미나 촉매의 제조 과정에 미치는 영향 연구", 2017 년 한국화학공학회 춘계학회, P 촉매목-10, 제주 ICC (2017/4/26-28).

2. **유재경**, 한승주, 박승원, 송지환, 송인규, "담지 과정에서 계면활성제를 도입한 니켈/알루미나 제로젤 촉매 상에서 천연가스의 수증기 개질 반응을 통한 수소 생산", 2016 년 한국화학공학회 추계학회, P 촉매금-34, 대전 DCC (2016/10/19-21).

3. **유재경**, 한승주, 박승원, 송지환, 송인규, "바나듐-니켈-알루미나 제로젤 촉매 상에서 천연가스의 수증기 개질 반응을 통한 수소 생산", 2016 년 한국화학공학회 춘계학회, P 촉매금-27, 부산 BEXCO (2016/4/27-29).

4. **유재경**, 한승주, 박승원, 송지환, 송인규, "Hollow sphere 구조를 갖는 니켈-알루미나 촉매 상에서의 메탄의 삼중 개질 반응", 2015 년

한국화학공학회 추계학술회의, P 촉매금-7, 일산 KINTEX (2015/10/21-23).

5. **유재경**, 방용주, 한승주, 박승원, 송지환, 송인규, “니켈-알루미나 에어로젤 촉매 상에서의 메탄의 삼중 개질 반응”, 2015 년 한국화학공학회 춘계학술회의, P 촉매목-4, 제주 ICC (2015/4/22-24).

6. **유재경**, 방용주, 한승주, 박승원, 송인규, “세리아를 담체로 이용한 니켈 촉매 상에서의 메탄의 삼중 개질 반응”, 2014 년 한국화학공학회 추계학술회의, P 촉매금-6, 대전 DCC (2014/10/22-24).

7. **유재경**, 방용주, 한승주, 송인규, “세리아가 포함된 중형기공성 니켈 촉매 상에서 메탄의 삼중 개질 반응을 통한 수소 가스 생산”, 2014 년 한국공업화학회 춘계학술회의, 1P-265, 제주 ICC (2014/4/30-5/2).

8. **유재경**, 방용주, 한승주, 송인규, “세리아의 도입이 니켈계 촉매 상에서의 메탄의 삼중 개질 반응에 미치는 영향”, 2014 년 한국화학공학회 춘계학술회의, P 촉매금-69, 창원 컨벤션센터 (2014/4/23-25).

9. **유재경**, 방용주, 한승주, 송인규, “중형기공성 니켈-알루미나 촉매 상의 액화천연가스의 수증기 개질 반응에 마그네슘 조촉매의 도입이 미치는 영향”, 2013 년 한국공업화학회 추계학술회의, 2P-179, 대전 컨벤션센터 (2013/10/30-11/1).

10. **유재경**, 방용주, 한승주, 송인규, “마그네슘을 조촉매로 첨가한 중형기공성 니켈-알루미나 촉매의 제조 및 액화천연가스(LNG)의 수증기 개질 반응으로의 적용”, 2013 년 한국화학공학회 추계학술회의, P 촉매목-9, 대구 EXCO (2013/10/23-25).

11. **유재경**, 방용주, 한승주, 서정길, 송인규, “중형기공성 M/니켈-알루미나(M=Mg, Ca, Sr 및 Ba) 촉매 상의 액화천연가스의 수증기 개질 반응을 통한 수소 가스 생산”, 2013 년 한국공업화학회 춘계학술회의, 1P-398, 제주 국제컨벤션센터 (2013/5/1-3).

12. **유재경**, 방용주, 한승주, 서정길, 송인규, “알칼리 토금속을 첨가한 중형기공성 니켈-알루미나 촉매의 제조 및 액화천연가스(LNG)의 수증기 개질 반응으로의 적용”, 2013 년 한국화학공학회 춘계학술회의, P 촉매금-10, 광주 김대중컨벤션센터 (2013/4/24-26).

Domestic conferences (Co-author)

1. 유상범, 송지환, **유재경**, 박승원, 송인규, “코발트/알루미늄-세륨 복합 산화물 촉매 상에서의 에탄올 수증기 개질 반응을 통한 수소 가스 생산”, 한국화학공학회 추계학술회의, P 촉매목-7, 대전 DCC (2017/10/25-27).

2. 송지환, 유상범, **유재경**, 박승원, 김민영, 김도희, 송인규, “니켈-코발트/알루미늄-란탄 산화물 이종금속 촉매 상에서의 에탄올 수증기 개질 반응을 통한 수소 가스 생산”, 한국화학공학회 추계학술회의, P 촉매목-5, 대전 DCC (2017/10/25-27).

3. 박승원, **유재경**, 송지환, 이어진, 유상범, 송인규, “조촉매로 몰리브데넘을 도입한 중형기공성 니켈계 제로젤 촉매 상에서 액화천연가스의 수증기 개질 반응을 통한 수소 가스 생산”, 한국화학공학회 추계학술회의, P 촉매목-1, 대전 DCC (2017/10/25-27).

4. 송지환, 유상범, **유재경**, 박승원, 김민영, 김도희, 송인규, “니켈/알루미늄-란탄 복합 산화물 촉매 상에서의 에탄올 수증기 개질 반응을 통한 수소 가스 생산”, 2017 년 한국화학공학회 춘계학회, P 촉매목-5, 제주 ICC (2017/4/26-28).

5. 박승원, **유재경**, 송지환, 이어진, 유상범, 송인규, “수소가스 생산을 위해 비금속 조촉매 붕소를 도입한 중형기공성 니켈계 상에서 액화천연가스의 수증기 개질 반응을 통한 수소 가스 생산”, 2017 년 한국화학공학회 춘계학회, P 촉매목-4, 제주 ICC (2017/4/26-28).

6. 강기혁, 한승주, 이종원, **유재경**, 박승원, 이어진, 송인규, “붕소가 첨가된 Re-Ru/C 촉매 상에서 숙신산의 수소화를 통한 1,4-부탄디올의 제조”, 2016 년 한국화학공학회 추계학회, P 촉매금-94, 대전 DCC (2016/10/19-21).

7. 한승주, 송지환, **유재경**, 박승원, 강기혁, 송인규, “정렬된 중형기공을 갖는 니켈-알루미나-지르코니아 상의 에탄올의 수증기 개질 반응을 통한 수소 가스 생산”, 2016 년 한국화학공학회 추계학회, P 촉매금-82, 대전 DCC (2016/10/19-21).

8. 박승원, 한승주, **유재경**, 송지환, 이어진, 송인규, “니켈-붕소-알루미나 제로젤 촉매 상에서 수소 가스 생산을 위한 액화천연가스의 수증기 개질 반응”, 2016 년 한국화학공학회 추계학회, P 촉매금-35, 대전 DCC (2016/10/19-21).

9. 송지환, 한승주, **유재경**, 박승원, 송인규, “니켈-스트론튬-알루미나-지르코니아 에어로젤 촉매 상에서의 에탄올 수증기 개질 반응을 통한 수소 가스 생산”, 2016 년 한국화학공학회 추계학회, P 촉매금-36, 대전 DCC (2016/10/19-21).

10. 한승주, 송지환, **유재경**, 박승원, 강기혁, 송인규, “칼슘이 도입된 중형기공성 코발트-알루미나 제로젤 촉매의 제조 및 에탄올 수증기 개질 반응으로의 적용”, 2016 년 한국화학공학회 춘계학회, P 촉매금-80, 부산 BEXCO (2016/4/27-29).

11. 박승원, 한승주, **유재경**, 송지환, 송인규, “비금속 조촉매로 붕소를 도입한 중형기공성 니켈-붕소-알루미나 제로젤 촉매 상에서 액화천연가스의 수증기 개질 반응을 통한 수소 가스 생산”, 2016 년 한국화학공학회 춘계학회, P 촉매금-28, 부산 BEXCO (2016/4/27-29).

12. 송지환, 한승주, **유재경**, 박승원, 송인규, “지르코니아 촉매 상에서 에탄올 수증기 개질 반응을 통한 수소 가스 생산”, 2016 년 한국화학공학회 춘계학회, P 촉매금-31, 부산 BEXCO (2016/4/27-29).

13. 강기혁, 한승주, 이종원, 강태훈, **유재경**, 송인규, “중형기공성 탄소 담체에 담지된 귀금속 촉매 상에서 숙신산의 수소화를 통한 1,4-부탄디올의 제조”, 2016 년 한국화학공학회 춘계학회, O 촉매 J 목-1, 부산 BEXCO (2016/4/27-29).

14. 한승주, 송지환, **유재경**, 박승원, 강기혁, 송인규. “스피넬 구조를 갖는 복합 알루미나 담체에 담지된 코발트 촉매 상의 에탄올 수증기 개질 반응을 통한 수소 가스 생산”, 2015 년 한국화학공학회 추계학술회의, P 촉매금-9, 일산 KINTEX (2015/10/21-23).

15. 송지환, 한승주, **유재경**, 박승원, 송인규, “알칼리 토금속 조촉매가 도입된 니켈/알루미나-지르코니아 촉매 상의 에탄올 수증기 개질 반응을 통한 수소 가스 생산”, 2015 년 한국화학공학회 추계학술회의, P 촉매금-10, 일산 KINTEX (2015/10/21-23).

16. 박승원, 송인규, 한승주, **유재경**, 송지환, “중형기공성 니켈-붕소-알루미나 제로젤 촉매 상의 액화천연가스 수증기 개질 반응을 통한 수소 가스 생산”, 2015 년 한국화학공학회 추계학술회의, P 촉매금-12, 일산 KINTEX (2015/10/21-23).

17. 박승원, 방용주, 한승주, **유재경**, 송지환, 송인규, “에폭사이드 기반 졸겔법으로 제조된 중형기공성 니켈-철-알루미나 제로젤 촉매 상의 액화천연가스 수증기 개질 반응을 통한 수소 가스 생산”, 2015 년 한국화학공학회 춘계학술회의, P 촉매목-3, 제주 ICC (2015/4/22-24).

18. 한승주, 방용주, **유재경**, 박승원, 송지환, 송인규, “단일공정 에폭사이드 기반 졸-겔법을 통해 제조된 니켈-구리-알루미나-지르코니아 제로젤 촉매를 이용한 에탄올 수증기 개질 반응에 대한 연구”, 2015 년 한국화학공학회 춘계학술회의, P 촉매목-5, 제주 ICC (2015/4/22-24).

19. 한승주, 방용주, **유재경**, 박승원, 송인규, “P123 과 이온성 액체가 주형물질로 도입된 중형기공성 니켈-알루미나 촉매 제조 및 에탄올 수증기 개질 반응으로의 적용”, 2014 년 한국화학공학회 추계학술회의, P 촉매금-4, 대전 DCC (2014/10/22-24).

20. 박승원, 방용주, 한승주, **유재경**, 송인규, “중형기공성 니켈-철-알루미나 제로젤 촉매 상의 액화천연가스 수증기 개질반응을 통한 수소가스 생산”, 2014 년 한국화학공학회 추계학술회의, P 촉매금-8, 대전 DCC (2014/10/22-24).

21. 방용주, 박승원, 한승주, **유재경**, 최정호, 송인규, “킬레이트화된 니켈 전구체의 함침을 통한 니켈/알루미나 촉매의 제조 및 액화천연가스의 수증기 개질 반응으로의 적용”, 2014 년 한국화학공학회 추계학술회의, P 촉매금-11, 대전 DCC (2014/10/22-24).

22. 한승주, 방용주, **유재경**, 서정길, 송인규, “P123 이 도입된 졸겔법을 통한 니켈-알루미나-지르코니아 제로젤 촉매 제조 및 에탄올 수증기 개질 반응으로의 적용”, 2014 년 한국공업화학회 춘계학술회의, 1P-254, 제주 ICC (2014/4/30-5/2).

23. 방용주, 한승주, **유재경**, 박승원, 최정호, 송인규, “탄소 입자를 주형 물질로 하는 중형기공성 니켈-인-알루미나 촉매의 제조 및 액화천연가스의 수증기 개질 반응으로의 적용”, 2014 년 한국공업화학회 춘계학술회의, 1P-256, 제주 ICC (2014/4/30-5/2).

24. 박승원, 방용주, 한승주, **유재경**, 송인규, “에폭사이드 기반 졸-겔법을 통해 제조된 니켈-철-알루미나 제로젤 촉매의 액화천연가스 수증기 개질 반응으로의 적용”, 2014 년 한국공업화학회 춘계학술회의, 1P-262, 제주 ICC (2014/4/30-5/2).

25. 한승주, 방용주, **유재경**, 서정길, 송인규, “P123 이 도입된 중형기공성 니켈-알루미나-지르코니아 제로젤 촉매 상에서 에탄올 수증기 개질 반응을 통한 수소 가스 생산”, 2014 년 한국화학공학회 춘계학술회의, P 촉매금-67, 창원 컨벤션센터 (2014/4/23-25).

26. 박승원, 방용주, 한승주, **유재경**, 송인규, “중형기공성 니켈-철-알루미나 제로젤 촉매 상의 액화천연가스의 수증기 개질 반응을 통한 수소 가스 생산”, 2014 년 한국화학공학회 춘계학술회의, P 촉매금-68, 창원 컨벤션센터 (2014/4/23-25).

27. 방용주, 한승주, **유재경**, 박승원, 최정호, 송인규,“인이 도입된 중형기공성 니켈-알루미나 촉매 상의 액화천연가스의 수증기 개질 반응”, 2014 년 한국화학공학회 춘계학술회의, O 촉매목-10, 창원 컨벤션센터 (2014/4/23-25).

28. 방용주, 한승주, **유재경**, 최정호, 송인규, “인이 도입된 중형기공성 니켈-인-알루미나 에어로젤 촉매의 제조 및 액화천연가스의 수증기 개질 반응으로의 적용”, 2013 년 한국공업화학회 추계학술회의, 2P-253, 대전 컨벤션센터 (2013/10/30-11/1).

29. 한승주, 방용주, **유재경**, 서정길, 송인규, “에탄올 수증기 개질 반응에서 니켈-알루미나-지르코니아 촉매에 도입된 계면활성제가 반응 활성에 미치는 영향”, 2013 년 한국공업화학회 추계학술회의, 2P-174, 대전 컨벤션센터 (2013/10/30-11/1).

30. 방용주, 한승주, **유재경**, 최정호, 송인규, “인이 도입된 중형기공성 니켈/알루미나 제어로젤 촉매 상의 액화천연가스의 수증기 개질 반응을 통한 수소 가스 생산”, 2013 년 한국화학공학회 추계학술회의, P 촉매목-2, 대구 EXCO (2013/10/23-25).

31. 한승주, 방용주, **유재경**, 서정길, 송인규. “계면활성제가 도입된 중형기공성 니켈-알루미나-지르코니아 제로젤 촉매 상에서 에탄올 수증기 개질 반응을 통한 수소 가스 생산”, 2013 년 한국화학공학회 추계학술회의, P 촉매목-3, 대구 EXCO (2013/10/23-25).

32. 방용주, 한승주, **유재경**, 서정길, 송인규, “인이 도입된 중형기공성 Ni-P_2O_5-Al_2O_3 제어로젤 촉매의 제조 및 액화천연가스의 수증기 개질 반응으로의 적용”, 2013 년 한국공업화학회 춘계학술회의, 1P-459, 제주 국제컨벤션센터 (2013/5/1-3).

33. 한승주, 방용주, **유재경**, 서정길, 송인규, “초임계 건조를 통해 제조한 니켈-알루미나-지르코니아 에어로젤 촉매의 에탄올 수증기 개질 반응으로의 적용”, 2013 년 한국공업화학회 춘계학술회의, 1P-401, 제주 국제컨벤션센터 (2013/5/1-3).

34. 방용주, 한승주, **유재경**, 서정길, 송인규, “기공팽창제가 도입된 중형기공성 니켈-알루미나 촉매 상의 액화천연가스의 수증기 개질 반응을 통한 수소 가스 생산”, 2013 년 한국화학공학회 춘계학술회의, O 촉매 I 목-23, 광주 김대중컨벤션센터 (2013/4/24-26).

35. 한승주, 방용주, **유재경**, 서정길, 송인규, “중형기공성 니켈-알루미나-지르코니아 에어로젤 촉매 상에서 에탄올 수증기 개질 반응을 통한 수소 가스 생산”, 2013 년 한국화학공학회 춘계학술회의, P 촉매금-6, 광주 김대중컨벤션센터 (2013/4/24-26).

36. 한승주, 방용주, **유재경**, 서정길, 윤민혜, 송인규, “에탄올 수증기 개질반응에서 중형기공성 니켈-알루미나-지르코니아 촉매의 니켈 담지량이 반응 활성에 미치는 영향”, 2012 년 한국공업화학회 추계학술회의, 2P-176, 대전컨벤션센터 (2012/10/31-11/2).

37. 방용주, 한승주, **유재경**, 서정길, 윤민혜, 송인규, “기공팽창제의 도입을 통한 정렬된 중형기공을 갖는 니켈-알루미나 촉매의 제조 및 액화천연가스의 수증기 개질 반응으로의 적용”, 2012 년 한국공업화학회 추계학술회의, 2P-179, 대전컨벤션센터 (2012/10/31-11/2).

38. 한승주, 방용주, **유재경**, 서정길, 윤민혜, 송인규, “단일공정 에폭사이드 기반 졸-겔법을 통해 제조된 니켈-알루미나-지르코니아 제어로젤 촉매를 이용한 에탄올 수증기 개질반응에 대한 연구”, 2012 년 한국화학공학회 추계학술회의, P 촉매수-12, 부산 BEXCO (2012/10/24-26).

39. 방용주, 한승주, **유재경**, 서정길, 윤민혜, 송인규, “정렬된 중형기공을 갖는 니켈-알루미나 촉매 상의 액화천연가스의 수증기 개질 반응을

통한 수소 가스 생산", 2012 년 한국화학공학회 추계학술회의, P 촉매수-15, 부산 BEXCO (2012/10/24-26).